A High-Order Finite-Difference Method on Staggered Curvilinear Grids for Seismic Wave Propagation Applications with Topography

Ossian O'Reilly[1], Te-Yang Yeh[2], Kim B. Olsen[*2], Zhifeng Hu[2], Alex Breuer[3], Daniel Roten[2], and Christine A. Goulet[1]

ABSTRACT

We developed a 3D elastic wave propagation solver that supports topography using staggered curvilinear grids. Our method achieves comparable accuracy to the classical fourth-order staggered grid velocity–stress finite-difference method on a Cartesian grid. We show that the method is provably stable using summation-by-parts operators and weakly imposed boundary conditions via penalty terms. The maximum stable timestep obeys a relationship that depends on the topography-induced grid stretching along the vertical axis. The solutions from the approach are in excellent agreement with verified results for a Gaussian-shaped hill and for a complex topographic model. Compared with a Cartesian grid, the curvilinear grid adds negligible memory requirements, but requires longer simulation times due to smaller timesteps for complex topography. The code shows 94% weak scaling efficiency up to 1014 graphic processing units.

KEY POINTS

- High-frequency seismic hazards can be significantly affected by topographic effects.
- We developed a provable stable 3D wave propagation solver supporting topography via curvilinear grids.
- Our method offers a computationally efficient approach to explore topographic effects on ground motions.

INTRODUCTION

Seismic modeling studies often successfully reproduce amplitudes and in many cases the phasing of observed ground motions for periods longer than about 2 s (e.g., Olsen *et al.*, 2003; Aagaard and Graves, 2011) using flat free surface approximations, conveniently implemented in numerical wave propagation methods, for example, using asymmetry of stresses and ghost layers in finite-difference (FD) methods (FDMs; Graves, 1996; Gottschämmer and Olsen, 2001). However, at higher frequencies, data indicate that surface topography could play an important role in ground-motion amplification. For example, Spudich *et al.* (1996) showed that the 1.78*g* acceleration recorded at station Tarzana from the 1994 Northridge earthquake was in part due to a factor-of-4.5 directional resonance amplification at 3.5 Hz of the sensor located on top of a 15-m-high hill. This trend is confirmed by simulations; for example, Rodgers *et al.* (2010) showed that topographic roughness has a dramatic effect on amplification of higher-frequency (2–8 Hz) waves generated from sources at the North Korean nuclear test site. In addition, ground-motion variability, an important factor in seismic hazard analysis, can be strongly affected by surface topography, as well as small-scale velocity perturbations in the crust (Imperatori and Mai, 2015). Thus, it is imperative to develop stable, accurate, and efficient support for topographic effects in 3D wave propagation and ground-motion estimation.

Our primary target application for topography support is an anelastic wave attenuation propagation code with suffix derived from the authors, Olsen, Day, and Cui (AWP-ODC), a numerical code developed to solve the viscoelastodynamic equations in a complex 3D medium. The code is highly scalable on both central processing unit and graphic processing unit (GPU) platforms, as demonstrated for large-scale simulations including TeraShake (Olsen *et al.*, 2006), TeraShake-2 (Olsen *et al.*,

1. Southern California Earthquake Center, University of Southern California, Los Angeles, California, U.S.A., https://orcid.org/0000-0002-9539-2582 (OOR); https://orcid.org/0000-0002-7643-357X (CAG); 2. Department of Geological Sciences, San Diego State University, San Diego, California, U.S.A., https://orcid.org/0000-0002-9146-6804 (T-YY); https://orcid.org/0000-0002-3078-485X (KBO); https://orcid.org/0000-0003-3835-8350 (ZH); 3. Faculty of Mathematics and Computer Science, Friedrich Schiller University Jena, Institute of Computer Science, Jena, Germany

*Corresponding author: kbolsen@sdsu.edu

Cite this article as O'Reilly, O., T.-Y. Yeh, K. B. Olsen, Z. Hu, A. Breuer, D. Roten, and C. A. Goulet (2021). A High-Order Finite-Difference Method on Staggered Curvilinear Grids for Seismic Wave Propagation Applications with Topography, *Bull. Seismol. Soc. Am.* **XX**, 1–20, doi: 10.1785/0120210096

2008), ShakeOut-D (Olsen *et al.*, 2009), and M8 (Cui *et al.*, 2010). AWP-ODC is also an important community modeling tool used to further knowledge of the dynamics and hazards of earthquakes and to support engineering research for safer building designs (Crouse *et al.*, 2018). AWP-ODC offers a computationally efficient approach to large-scale numerical wave propagation, in part due to favorable numerical dispersion properties derived from the fourth-order staggered grid (SG) FD stencils. In addition to computational efficiency, AWP-ODC does not require any mesh generation, unlike unstructured mesh methods such as finite elements (e.g., Tu *et al.*, 2006), spectral elements (e.g., Komatitsch and Vilotte, 1998), and discontinuous Galerkin (DG) methods (e.g., Käser and Dumbser, 2008; Etienne *et al.*, 2010; Chung *et al.*, 2015; Breuer *et al.*, 2017). These aspects make AWP-ODC an appropriate target application for exploring ground-motion effects from topographic scattering.

A wide variety of approaches have been proposed to implement irregular surface topography into the SGFD method; we list a few examples later. Takenaka *et al.* (2009) presented an image condition to implement both land topography and liquid–solid topography in a fourth-order SGFD code. Mittet (2002), Zeng *et al.* (2012), and Kristek *et al.* (2016) assigned elastic parameters and density above the free surface to approximate a vacuum formulation in different ways, either by including tapering or averaging or by scaling the elastic moduli. Peskin (1972) developed the immersed-boundary method that attempts to satisfy the traction-free condition by combining ghost grid values beyond the free surface by interpolation, followed later by solvers from Almuhaidib and Toksöz (2015) and Bayliss *et al.* (1986). Unfortunately, these approaches suffer from stability issues or need a resolution that renders them inhibitive for realistic models and frequency ranges, such as those required for engineering applications.

Curvilinear grids represent a somewhat different class of approaches to implement irregular topography into SGFD schemes (e.g., Lombard *et al.*, 2008; Hu, 2016). Several researchers have proposed curvilinear approaches using collocated grids (e.g., Zhang *et al.*, 2012; Sun *et al.*, 2018). The nature of SGs presents a particular challenge for implementing curvilinear grids due to the distribution of wavefield variables throughout grid elements. In Hestholm and Ruud (1994, 1998, 2002), the authors use the classic staggered formulation and low-order interpolation to discretize the additional terms consistently. However, this method does not preserve the original SGFD scheme's accuracy and may suffer from instabilities in long duration problems (Hestholm, 2003). Some of the challenges due to SGs have been circumvented by mimetic grids (e.g., de la Puente *et al.*, 2014) or by rotating the grid (e.g., Saenger and Bohlen, 2004) to partially collocate the stresses and velocities. However, Saenger and Bohlen (2004) found that rotated SGs require a significantly finer discretization of irregular topography for the same accuracy compared with standard SGs, making the technique less practical.

In this work, we discretize the elastic wave equation in the first-order form on a staggered curvilinear grid using high-order summation-by-parts (SBP) FD operators to develop an accurate and energy-conserving numerical method. The SBP approach forms a general framework for developing and analyzing the stability of many numerical schemes across various scientific and engineering applications. SBP operators with weakly imposed boundary conditions via the simultaneous approximation term (SAT) penalty technique (Carpenter *et al.*, 1994) lead to energy-stable schemes for many well-posed problems. The SBP-SAT approach enables energy stable multiblock, nonconforming structured grid (Mattsson and Carpenter, 2010) and unstructured-to-structured grid couplings (Kozdon and Wilcox, 2016; Lundquist *et al.*, 2018). The approach extends beyond FDMs and applies to other numerical methods, for example, finite volume (Nordström *et al.*, 2003), spectral element DG (Gassner, 2013), and flux reconstruction (Ranocha *et al.*, 2018). See also Svärd and Nordström (2014) and Fernández *et al.* (2014) for a review of the SBP-SAT approach.

In the context of computational seismology, the SBP approach has previously been used to develop energy-stable and high-order FD methods on collocated curvilinear grids in both first- and second-order forms of the acoustic and elastic wave equations using both central differencing and upwinding (Sjögreen and Petersson, 2012; Kozdon *et al.*, 2013; Dovgilovich and Sofronov, 2015; Duru and Dunham, 2016). SBP operators that enable energy-stable and energy-conservative discretizations of wave equations on SGs were introduced in O'Reilly *et al.* (2017) and extended to curvilinear grids in O'Reilly and Petersson (2020), nonconforming grid coupling in Gao *et al.* (2019), and FEM-SGFD coupling in Gao and Keyes (2019).

Although many of the traditional SGFD approaches rely on ghost points and mirroring to impose the traction-free boundary condition in the elastic wave equation, we weakly impose it via SAT terms. Unlike collocated grids or partially SG approaches, our approach must treat additional terms that cannot be naturally discretized on an SG. We do so using high-order interpolation and achieve comparable accuracy to the classic SGFD scheme, while also preserving its computational efficiency. Because the method is provably energy conservative, it can handle any smooth topography without producing instability as long as the timestep is sufficiently small.

This article is arranged as follows. First, we describe the curvilinear grid approach used to support irregular topography, including its implementation in the fourth-order AWP SGFD code. We then analyze the stability of the method and verify the accuracy of the method for a Gaussian hill and a realistically complex topographic model. Finally, we summarize the method and its application in simulations of 3D wave propagation in complex media. A discussion of the energy balance for the elastic wave equation is provided in Appendix A and application to the semidiscrete problem in Appendix B.

PROBLEM FORMULATION

Consider the elastic wave equation in Cartesian coordinates for a linear isotropic material posed on a domain Ω in 3D:

$$\rho \frac{\partial v_i}{\partial t} = \sum_{j=1}^{3} \frac{\partial \sigma_{ij}}{\partial x_j}, \tag{1}$$

$$\frac{\partial \sigma_{ij}}{\partial t} = \lambda \sum_{k=1}^{3} \frac{\partial v_k}{\partial x_k} \delta_{ij} + \mu \left(\frac{\partial v_i}{\partial x_j} + \frac{\partial v_j}{\partial x_i} \right), \tag{2}$$

for $i = 1, 2, 3$, $j = 1, 2, 3$. In equations (1) and (2), x_i are Cartesian coordinates, $\rho > 0$ is the density, $\mu > 0$ is the shear modulus, $\lambda > 0$ is Lamé's first parameter, v_i are the components of the particle velocity field, and σ_{ij} are the components of the symmetric stress tensor, $\sigma_{ij} = \sigma_{ji}$. Our index notation does not sum repeated indexes.

Although most seismic wave propagation applications require some way of absorbing outgoing waves at exterior boundaries, for example, sponge layers (Cerjan *et al.*, 1985), absorbing boundary conditions (Givoli *et al.*, 2006), perfectly matched layers (Berenger, 1994; Olsen and Marcinkovich, 2003), and super grid (Appelö and Colonius, 2009), we focus exclusively on imposing a traction-free boundary condition in this study.

On the exterior boundary $\partial\Omega$, we prescribe the traction-free boundary condition

$$\mathbf{T} = \mathbf{0}, \quad (x_1, x_2, x_3) \in \partial\Omega, \tag{3}$$

in which $\mathbf{T}$ is the traction vector. The Cartesian components of the traction vector are

$$T_i = \sum_j \sigma_{ij} n_j, \tag{4}$$

in which n_j are the Cartesian components of the outward pointing unit normal with respect to $\partial\Omega$. Our approach to implement this traction-free boundary using a curvilinear grid is described in the following.

The elastic wave equation in curvilinear coordinates

We first review some of the key concepts for working with curvilinear coordinate transforms (Thompson *et al.*, 1998; Grinfeld, 2013). Let (r^1, r^2, r^3) denote curvilinear coordinates that satisfy $0 \le r^i \le 1$ for $i = 1, 2, 3$. The superscripts i are *contravariant* indexes, not powers. The Cartesian coordinates map to the curvilinear coordinates via

$$x_1 = F_1(r^1, r^2, r^3), \quad x_2 = F_2(r^1, r^2, r^3), \quad x_3 = F_3(r^1, r^2, r^3).$$

We assume that this mapping is continuously differentiable, nonsingular, and one-to-one. By differentiating the mapping with respect to the curvilinear coordinates, we obtain the *covariant basis*

$$\mathbf{a}_i = \begin{bmatrix} \frac{\partial x_1}{\partial r^i} \\ \frac{\partial x_2}{\partial r^i} \\ \frac{\partial x_3}{\partial r^i} \end{bmatrix}, \quad a_{ij} = \frac{\partial x_j}{\partial r^i}, \quad i = 1, 2, 3, \quad j = 1, 2, 3. \tag{5}$$

The covariant basis vectors are tangential to the grid lines spanned by the curvilinear coordinates.

Let $\mathbf{a}^i$ denote the contravariant base vectors that are defined by the orthogonality relationship

$$\mathbf{a}_i \cdot \mathbf{a}^j = \delta_{ij}, \quad \mathbf{a}^j = \begin{bmatrix} \frac{\partial r^j}{\partial x_1} \\ \frac{\partial r^j}{\partial x_2} \\ \frac{\partial r^j}{\partial x_3} \end{bmatrix}, \quad a^{ji} = \frac{\partial r^j}{\partial x_i}, \quad i = 1, 2, 3, \quad j = 1, 2, 3, \tag{6}$$

in which δ_{ij} is the Kronecker delta and $\mathbf{a1} \cdot \mathbf{a2}$ is the dot product. The determinant of the Jacobian J of the curvilinear mapping is

$$J = \mathbf{a}_1 \cdot (\mathbf{a}_2 \times \mathbf{a}_3) = \mathbf{a}_2 \cdot (\mathbf{a}_3 \times \mathbf{a}_1) = \mathbf{a}_3 \cdot (\mathbf{a}_1 \times \mathbf{a}_2) > 0. \tag{7}$$

In equation (7), $\mathbf{a}_1 \times \mathbf{a}_2$ is the cross product and $\mathbf{a}_1 \cdot \mathbf{a}_2$ is the dot product. Because the covariant base vectors are tangential to the curvilinear grid lines, we can find the normal with respect to the boundary. For example, the outward pointing unit normal on the top boundary is

$$\mathbf{n} = \frac{\mathbf{a}_1 \times \mathbf{a}_2}{|\mathbf{a}_1 \times \mathbf{a}_2|}, \quad r^3 = 1. \tag{8}$$

In equation (8), $|\cdot|$ denotes the Euclidean norm in 3D, that is, $|\mathbf{x}| = \sqrt{x_1^2 + x_2^2 + x_3^2}$.

Next, we derive a curvilinear formulation of the governing equations that is suitable for discretization. For this purpose, we need to transform the partial derivatives in the governing equations from Cartesian to curvilinear coordinates. To obtain a provably stable method, we need to combine partial derivative transforms of stresses and velocities. Following Duru and Dunham (2016), we transform the partial derivatives of the stress components using the *conservative form*

$$\begin{aligned} \frac{\partial \sigma_{ij}}{\partial x_j} &= \frac{1}{J} \left(\frac{\partial}{\partial r^1} \left(J \frac{\partial r^1}{\partial x_j} \sigma_{ij} \right) \right) + \frac{1}{J} \left(\frac{\partial}{\partial r^2} \left(J \frac{\partial r^2}{\partial x_j} \sigma_{ij} \right) \right) \\ &\quad + \frac{1}{J} \left(\frac{\partial}{\partial r^3} \left(J \frac{\partial r^3}{\partial x_j} \sigma_{ij} \right) \right) \\ &= \frac{1}{J} \sum_{k=1}^{3} \left(\frac{\partial}{\partial r^k} \left(J a^{kj} \sigma_{ij} \right) \right). \end{aligned} \tag{9}$$

We transform the partial derivatives of the velocity components by the chain rule

$$\frac{\partial v_j}{\partial x_i} = \frac{\partial v_j}{\partial r^1} \frac{\partial r^1}{\partial x_i} + \frac{\partial v_j}{\partial r^2} \frac{\partial r^2}{\partial x_i} + \frac{\partial v_j}{\partial r^3} \frac{\partial r^3}{\partial x_i} = \sum_{k=1}^{3} \frac{\partial v_j}{\partial r^k} a^{ki}. \tag{10}$$

The details of the discretization of equations (9) and (10) on an SG are critical for producing an accurate and stable numerical scheme. By transforming equations (1) and (2) using equations (9) and (10), respectively, we get

$$\rho \frac{\partial v_i}{\partial t} = \frac{1}{J} \sum_{k,j} \frac{\partial}{\partial r^k} (J a^{kj} \sigma_{ij}), \tag{11}$$

$$\frac{\partial \sigma_{ij}}{\partial t} = \lambda \sum_{k,l} \frac{\partial v_k}{\partial r_l} a^{lk} \delta_{ij} + \mu \sum_{l} \left(\frac{\partial v_i}{\partial r^l} a^{lj} + \frac{\partial v_j}{\partial r^l} a^{li} \right). \tag{12}$$

To demonstrate some of the challenges that we face when developing the numerical method, we expand all terms in equations (11) and (12):

$$\begin{aligned} \rho \frac{\partial v_i}{\partial t} = & \frac{1}{J} \left(\frac{\partial}{r^1} (J a^{11} \sigma_{i1}) + \frac{\partial}{r^2} (J a^{21} \sigma_{i1}) + \frac{\partial}{r^3} (J a^{31} \sigma_{i1}) \right) \\ & + \frac{1}{J} \left(\frac{\partial}{r^1} (J a^{12} \sigma_{i2}) + \frac{\partial}{r^2} (J a^{22} \sigma_{i2}) + \frac{\partial}{r^3} (J a^{32} \sigma_{i2}) \right) \\ & + \frac{1}{J} \left(\frac{\partial}{r^1} (J a^{13} \sigma_{i3}) + \frac{\partial}{r^2} (J a^{23} \sigma_{i3}) + \frac{\partial}{r^3} (J a^{33} \sigma_{i3}) \right), \end{aligned} \tag{13}$$

$$\begin{aligned} \frac{\partial \sigma_{ij}}{\partial t} = & \lambda \left(\left(\frac{\partial v_1}{\partial r_1} a^{11} + \frac{\partial v_1}{\partial r_2} a^{21} + \frac{\partial v_1}{\partial r_3} a^{31} \right) \right. \\ & + \left(\frac{\partial v_2}{\partial r_1} a^{12} + \frac{\partial v_2}{\partial r_2} a^{22} + \frac{\partial v_2}{\partial r_3} a^{32} \right) \\ & \left. + \left(\frac{\partial v_3}{\partial r_1} a^{13} + \frac{\partial v_3}{\partial r_2} a^{23} + \frac{\partial v_3}{\partial r_3} a^{33} \right) \right) \delta_{ij} \\ & + \mu \left(\left(\frac{\partial v_i}{\partial r^1} a^{1j} + \frac{\partial v_i}{\partial r^2} a^{2j} + \frac{\partial v_i}{\partial r^3} a^{3j} \right) \right. \\ & \left. + \left(\frac{\partial v_j}{\partial r^1} a^{1i} + \frac{\partial v_j}{\partial r^2} a^{2i} + \frac{\partial v_j}{\partial r^3} a^{3i} \right) \right). \end{aligned} \tag{14}$$

The curvilinear formulation of the elastic wave equation recovers the Cartesian formulation if the mapping satisfies $a^{kj} = \delta_{kj}$ and $J = 1$. Hence, a general curvilinear formulation includes six additional terms per velocity component equation, four per shear stress component equation, and 10 per normal stress component equation. The terms containing a^{kk} are the *diagonal terms*. Because these terms are present in the Cartesian formulation, they are straightforward to discretize. The *off-diagonal terms*, a^{kj}, $k \neq j$, cannot be naturally represented in the SG. When we construct the numerical scheme, we accurately discretize the off-diagonal terms by combining interpolation and difference operators.

Weakly imposed boundary conditions

In constructing the numerical scheme, we only approximately satisfy the traction-free boundary condition, imposed by a *penalty term* acting on the right side of the momentum balance equations. The role of the penalty term is to drive the numerical solution on the boundary toward satisfying the boundary condition. The penalty term depends on one or more real-valued weights that must be chosen such that the scheme is stable.

The construction and analysis of penalty terms can be more easily done and understood in the continuous setting first. To weakly impose the boundary condition (equation 3), we add the following penalty term to equation (11)

$$\rho \frac{\partial v_i}{\partial t} = \frac{1}{J} \sum_{k,j} \frac{\partial}{\partial r^k} (J a^{kj} \sigma_{ij}) - s_i, \tag{15}$$

in which

$$s_i = \alpha \mathcal{L}(T_i). \tag{16}$$

In equation (16), α is the penalty weight. In Appendix B, we show that this weight must be $\alpha = 1$ to conserve energy. In addition, $\mathcal{L}$ is a *lifting operator* (Arnold *et al.*, 2002; Janivita Joto Sudirham *et al.*, 2003) that converts a volume integral into a surface integral

$$\int_{\Omega} v_i \mathcal{L}(T_i) dV = \int_{\partial\Omega} v_i T_i dS. \tag{17}$$

In equation (17), dV is the infinitesimal volume element of Ω and dS is the infinitesimal element of the surface area of $\partial\Omega$. The formulation in equations (12)–(15) is the starting point for the construction of the numerical scheme, which is presented in the Numerical Method section.

NUMERICAL METHOD

Our numerical method for discretizing equations (12)–(15) uses the SBP SGFD operators developed in O'Reilly and Petersson (2020). We begin by reviewing the SBP SGFD method in 1D, followed by its extension to 3D. In particular, we focus on the discretization of the conservative and nonconservative forms of the partial derivative formulas in equations (9) and (10) in an energy-conserving manner.

SBP operators in 1D

In 1D, we discretize the interval $0 \leq r \leq 1$ using $N + 1$ equidistant grid points, including the boundary points, into the grid vector,

$$\mathbf{r} = [r_0 r_1 \ \ldots \ r_N]^T, \quad r_i = ih, i = 0, 1, \ldots, N, \quad h = \frac{1}{N}.$$

We also introduce a grid vector of length $N + 2$ that collects mid points and boundary points,

$$\hat{\mathbf{r}} = [\hat{r}_0 \hat{r}_1 \ldots \hat{r}_{N+1}]^T, \ \hat{r}_0 = 0, \ \hat{r}_i = \left(i - \frac{1}{2} \right) h, \ \hat{r}_{N+1} = 1, \quad i = 1, \ldots, N.$$

The velocity and stress field components $v(r,t)$ and $\sigma(r,t)$, respectively, are approximated at the nodal and cell-centered grid points by the grid functions $v_i = v(r_i,t)$ and $\sigma_i = \sigma(\hat{r}_i,t)$. The grid values are collected in the vectors $\boldsymbol{v} = [v_0 v_1 \ldots v_N]^T$ and $\boldsymbol{\sigma} = [\sigma_0 \sigma_1 \ldots \sigma_{N+1}]^T$.

The curvilinear formulation of the governing equations (11) and (12) has a special symmetry. For the momentum in the velocity equation (11), only the stress components (equation 12) occur on the right side. The opposite pattern is true for the stress equations. This symmetry allows us to approximate the first derivative of stress at the grid points that contain the velocity grid values, and vice versa. Let $\mathbf{D}$ denote a SBP FD operator that acts on a grid function stored at the cell-centered values and approximates the derivative at the nodal grid points. Likewise, let $\hat{\mathbf{D}}$ denote an FD operator that acts on a grid function stored at the nodal values and approximates the derivative at the cell-centered grid points. These difference operators result in the following approximations

$$\mathbf{D}\boldsymbol{\sigma} \approx \begin{bmatrix} \left(\frac{\partial \sigma}{\partial r}\right)_{r_0} \\ \left(\frac{\partial \sigma}{\partial r}\right)_{r_1} \\ \vdots \\ \left(\frac{\partial \sigma}{\partial r}\right)_{r_N} \end{bmatrix} \quad \text{and} \quad \hat{\mathbf{D}}\boldsymbol{v} \approx \begin{bmatrix} \left(\frac{\partial v}{\partial r}\right)_{\hat{r}_0} \\ \left(\frac{\partial v}{\partial r}\right)_{\hat{r}_1} \\ \vdots \\ \left(\frac{\partial v}{\partial r}\right)_{\hat{r}_{N+1}} \end{bmatrix}.$$

Because of the different number of grid points in each grid defined by stresses and velocities, the difference approximations form rectangular matrices. Each row in the matrices contains the coefficients in an unknown FD stencil. The first few points, including the boundary points, contain one-sided FD stencils; all of the rows for the interior grid points contain the same central FD stencil.

The one-sided boundary stencils are accurate to order p and the interior stencil is accurate to order $2p$. In this work, we use SBP operators that satisfy $p = 2$ (the second-order boundary accuracy and the fourth-order interior accuracy). In this case, the operators $\mathbf{D}$ and $\hat{\mathbf{D}}$ differentiate any constant, linear, and quadratic functions exactly (to machine precision), for example,

$$\hat{\boldsymbol{\xi}} = 2\mathbf{r}, \quad \hat{\mathbf{D}}\boldsymbol{\xi} = 2\hat{\mathbf{r}}, \quad \boldsymbol{\xi} = [r_0^2 r_1^2 \ldots r_N^2]^T, \quad \hat{\boldsymbol{\xi}} = [\hat{r}_0^2 \hat{r}_1^2 \ldots \hat{r}_{N+1}^2]^T. \tag{18}$$

In addition to accuracy constraints, the SBP operators satisfy constraints that allow them to approximate the integration by parts formula

$$\int_0^1 \sigma \frac{\partial v}{\partial r} dr = -\int_0^1 v \frac{\partial \sigma}{\partial r} dr + v(1,t)\sigma(1,t) - v(0,t)\sigma(0,t). \tag{19}$$

By construction, the SBP operators approximate equation (19) using the SBP formula

$$\boldsymbol{\sigma}^T \hat{\mathbf{H}} \hat{\mathbf{D}} \boldsymbol{v} = -\boldsymbol{v}^T \mathbf{H} \mathbf{D} \boldsymbol{\sigma} + v_N \sigma_{N+1} - v_0 \sigma_0. \tag{20}$$

This approximation holds the key to proving stability with SBP difference operators and is valid for any grid vectors $\boldsymbol{\sigma}$ and $\boldsymbol{v}$ of appropriate sizes. In equation (20), the diagonal matrices $\mathbf{H}$ and $\hat{\mathbf{H}}$ define quadrature rules with positive weights. These quadrature rules are accurate for degree $2p-1$ polynomials (Prochnow *et al.*, 2017). The SBP property can also be written as a matrix relationship

$$\hat{\mathbf{H}} \hat{\mathbf{D}} = -(\mathbf{H}\mathbf{D})^T + \hat{\mathbf{B}}, \quad \hat{\mathbf{B}} = \mathbf{B}^T = \hat{\mathbf{e}}_{N+1}\mathbf{e}_N^T - \hat{\mathbf{e}}_0 \mathbf{e}_0^T, \tag{21}$$

in which $\mathbf{e}_0 = [1 \;\; 0 \;\ldots\; 0]^T$, $\mathbf{e}_N = [0 \;\ldots\; 0 \;\; 1]^T$ such that $v_0 = \mathbf{e}_0^T \boldsymbol{v}$, $v_N = \mathbf{e}_N^T \boldsymbol{v}$, and so forth.

Let $\mathbf{P}$ and $\hat{\mathbf{P}}$ be SBP interpolation operators, defined analogously to $\mathbf{D}$ and $\hat{\mathbf{D}}$, respectively. In the interior of these operators, we use a central cubic interpolation formula. For a few grid points near the boundary, we use linear interpolation formulas. Thus, the operators interpolate any constant and linear functions exactly (to machine precision), for example,

$$\mathbf{P}\hat{\mathbf{r}} = \mathbf{r}, \quad \hat{\mathbf{P}}\mathbf{r} = \hat{\mathbf{r}}. \tag{22}$$

Similar to the integration by parts property, the interpolation operators also approximate an integral relationship. In the continuous setting, σ and v commute, and therefore

$$\int_0^1 \sigma v dr = \int_0^1 v \sigma dr.$$

Although commutativity does not necessarily hold in the discrete case, the SBP interpolation operators preserve this property,

$$\boldsymbol{\sigma}^T \hat{\mathbf{H}} \hat{\mathbf{P}} \boldsymbol{v} = \boldsymbol{v}^T \mathbf{H} \mathbf{P} \boldsymbol{\sigma}, \quad \hat{\mathbf{H}} \hat{\mathbf{P}} = (\mathbf{H}\mathbf{P})^T. \tag{23}$$

SBP operators in 3D

The grid values of the velocity and stress components are extended to 3D as shown in Figure 1a. All of these values are collected in the corresponding grid vectors $\boldsymbol{v}_i$ and $\boldsymbol{\sigma}_{ij}$. This arrangement coincides with the traditional SG formulation for an interior grid cell (Levander, 1988; Graves, 1996). However, because of the use of grid lines $\hat{r}_k$ that include boundary points, each stress and velocity component has a grid value on the boundary (Fig. 1b,c). For example, consider the boundary cell in Figure 1b. Here, the normal stress components are stored at both the cell center and the center of the face on the boundary.

The extension of the SBP operators to 3D follows by applying them grid line by grid line in each direction. Let $\mathbf{D}_k$ denote differentiation along each grid line in the r^k direction. Although operators that act in different directions always commute, for example, $\mathbf{D}_1 \hat{\mathbf{P}}_2 = \hat{\mathbf{P}}_2 \mathbf{D}_1$, those acting in the same direction do not commute, for example, $\mathbf{D}_1 \hat{\mathbf{P}}_1 \neq \hat{\mathbf{P}}_1 \mathbf{D}_1$. In Figure 1a, we can always infer from context if a difference

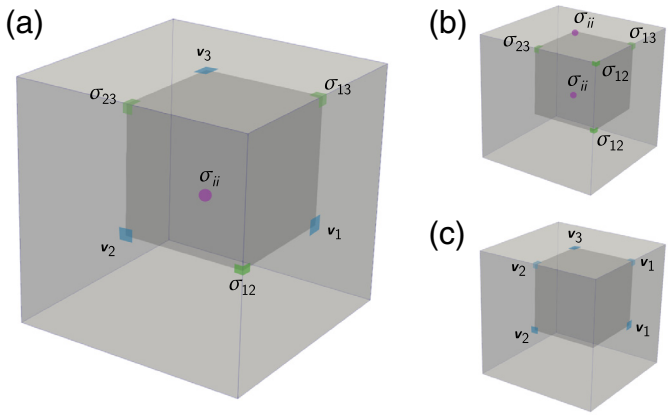

Figure 1. Arrangement of stress and velocity components within the first octant of a grid cell. (a) Grid cell in the interior, and grid cell on the boundary for (b) stress components and (c) velocity components. The color version of this figure is available only in the electronic edition.

operator acts on a grid function defined at cell-centered grid points or nodal grid points. For example, to differentiate $\boldsymbol{\sigma}_{13}$ in the r^3 direction we must use $\hat{\mathbf{D}}_3\boldsymbol{\sigma}_{13}$ because the grid values of $\boldsymbol{\sigma}_{13}$ in the r^3 direction are defined at the nodal grid points. To simplify the presentation of the numerical scheme, we infer from context what type of operator to use and introduce the following conventions. Let $\boldsymbol{\mathcal{D}}_k$ and $\hat{\boldsymbol{\mathcal{D}}}_k$ be difference operators that act on any $\boldsymbol{\sigma}_{ij}$ and $\boldsymbol{vi}$, respectively, in the r^k direction. The interpolation operators, $\boldsymbol{\mathcal{P}}_k$ and $\hat{\boldsymbol{\mathcal{P}}}_k$, adopt the same conventions. In 3D and with this notation, the SBP properties in equations (21) and (23) become

$$\hat{\boldsymbol{\mathcal{H}}}_k\hat{\boldsymbol{\mathcal{D}}}_k = -(\mathcal{H}_k\boldsymbol{\mathcal{D}}_k)^T + \hat{\boldsymbol{\mathcal{B}}}_k, \quad \hat{\boldsymbol{\mathcal{B}}}_k = \boldsymbol{\mathcal{B}}_k^T, \tag{24}$$

$$\hat{\boldsymbol{\mathcal{H}}}_k\hat{\boldsymbol{\mathcal{P}}}_k = (\boldsymbol{\mathcal{H}}_k\boldsymbol{\mathcal{P}}_k)^T. \tag{25}$$

Discretization of the partial derivatives

In this section, we describe the key steps in the discretization of the partial derivatives for our energy conservative high-order-accurate numerical method. Interested readers are referred to Appendices A and B for the complete analysis.

Two primary challenges occur when discretizing these terms:

- The approximation must be consistent at all grid points. This constraint requires a mix of interpolation and differentiation.
- To conserve energy in the discrete case, the order of operations becomes important. This is because matrices do not necessarily commute.

Given the large numbers of terms in equations (13) and (14) that we must discretize, it is convenient to analyze a simpler set of equations.

We consider the elastic wave equation in quasi-1D form, having $v_1(x_3, t)$ and $\sigma_{13}(x_3, t)$ as the only nonzero components. In this case, equations (13) and (14) simplify to

$$\rho\frac{\partial v_1}{\partial t} = \frac{1}{J}\left(\frac{\partial}{\partial r^1}(Ja^{13}\sigma_{13}) + \frac{\partial}{\partial r^2}(Ja^{23}\sigma_{13}) + \frac{\partial}{\partial r^3}(Ja^{33}\sigma_{13})\right), \tag{26}$$

$$\frac{\partial \sigma_{13}}{\partial t} = \mu\left(\frac{\partial v_1}{\partial r^1}a^{13} + \frac{\partial v_1}{\partial r^2}a^{23} + \frac{\partial v_1}{\partial r^3}a^{33}\right). \tag{27}$$

To accurately form a semidiscrete approximation for these equations, we must take into account how the fields v_1 and σ_{13} are staggered with respect to each other in space. Let us form a consistent semidiscrete approximation of equation (26) first. The first partial derivative term $\frac{1}{J}\frac{\partial}{\partial r^1}(Ja^{13}\sigma_{13})$ cannot be naturally discretized on the SG. If we only approximate this partial derivative term by a difference operator in the r^1 direction, $\boldsymbol{\mathcal{D}}_1$, the resulting approximation is accurate in the wrong location —at the v_3 grid location (see Fig. 1). Since the approximation must be accurate at the v_1 grid location, we first interpolate σ_{13} to the cell center (normal stress grid location) and then apply a difference approximation in the r^1 direction to obtain an accurate approximation at the desired grid location. To interpolate σ_{13} to the cell center, we interpolate all values along each grid line in the r^3 direction using $\boldsymbol{\mathcal{P}}_3$ and then interpolate the result along each grid line in the r^1 direction using $\boldsymbol{\mathcal{P}}_1$. A further complication is that we must also discretize the metric term Ja^{13}; we have chosen to discretize this term at the v_1 grid location, but other choices are also possible. We apply a similar strategy to discretize the second term. The third term is the diagonal term that appears in the Cartesian formulation of the elastic wave equation, and therefore it can be naturally discretized on the SG.

By applying the strategy outlined earlier, our semidiscrete approximation of equation (26) becomes

$$\boldsymbol{\rho}\frac{d\mathbf{v}_1}{dt} = (\mathbf{J}^{-1})_1\boldsymbol{\mathcal{D}}_1\boldsymbol{\mathcal{P}}_1(\mathbf{Ja}^{13})_1\boldsymbol{\mathcal{P}}_3\boldsymbol{\sigma}_{13} + (\mathbf{J}^{-1})_1\boldsymbol{\mathcal{D}}_2\boldsymbol{\mathcal{P}}_2(\mathbf{Ja}^{23})_1\boldsymbol{\mathcal{P}}_3\boldsymbol{\sigma}_{13} + (\mathbf{J}^{-1})_1\boldsymbol{\mathcal{D}}_3(\mathbf{Ja}^{33})_{13}\boldsymbol{\sigma}_{13}. \tag{28}$$

As previously mentioned, equation (28) mixes interpolation and differentiation to guarantee that the approximation is consistent at the $\boldsymbol{v}_1$ grid values. Figure 2 shows the actions performed by chaining together interpolation and differentiation operators for selected cases. In our notation, $(\mathbf{J}^{-1})_1$ contains the values of the reciprocal of the Jacobian determinant evaluated at the same grid points as the $\boldsymbol{v}_1$ grid values. Likewise, $(\mathbf{Ja}^{33})_{13}$ is evaluated at the same grid points as the $\boldsymbol{\sigma}_{13}$ grid values.

Next, consider the following semidiscrete approximation of equation (27):

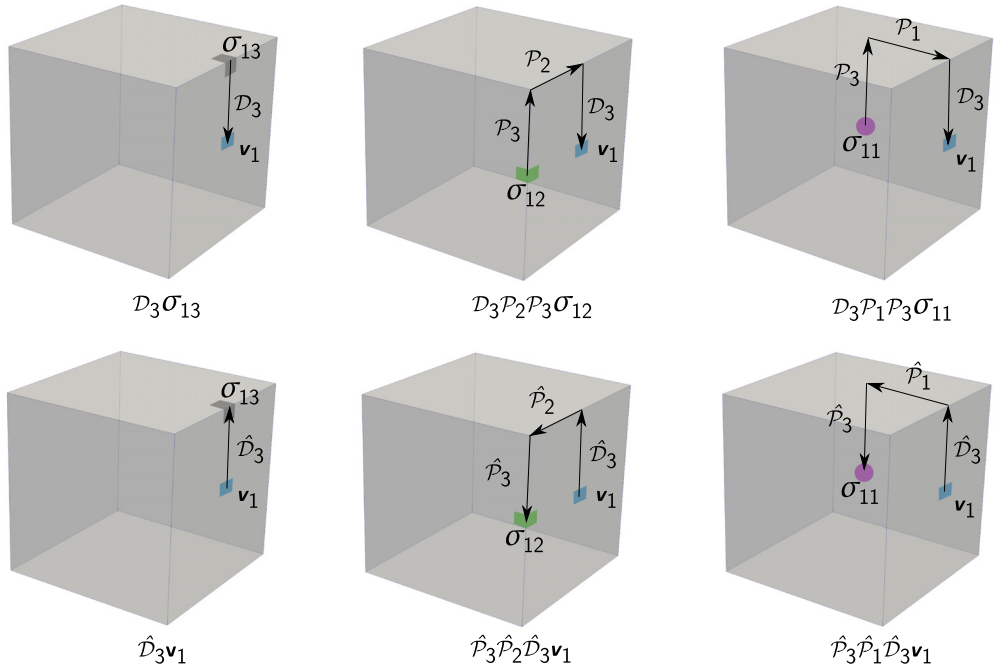

Figure 2. Interpolation and differentiation of stresses and velocities in a grid cell. Arrows point to where the approximation is evaluated. $\mathcal{D}_k$ and $\hat{\mathcal{D}}_k$ are difference operators that act on any $\boldsymbol{\sigma}_{ij}$ and $\boldsymbol{v}_i$, respectively, in the r^k direction, and $\mathcal{P}_k$ and $\hat{\mathcal{P}}_k$ are interpolation operators adopting the same conventions. To construct summation-by-parts (SBP) energy-conserving approximations, the order of interpolation and differentiation must be reversed for stresses compared with velocities, and vice versa. The color version of this figure is available only in the electronic edition.

$$\frac{d\boldsymbol{\sigma}_{13}}{dt} = \boldsymbol{\mu}_{13}((\mathbf{J}^{-1})_{13}\hat{\mathcal{P}}_3(\mathbf{J}\mathbf{a}^{13})_1\hat{\mathcal{P}}_1\hat{\mathcal{D}}_1\boldsymbol{v}_1 + (\mathbf{J}^{-1})_{13}\hat{\mathcal{P}}_3(\mathbf{J}\mathbf{a}^{23})_1\hat{\mathcal{P}}_2\hat{\mathcal{D}}_2\boldsymbol{v}_1 + (\mathbf{a}^{33})_{13}\hat{\mathcal{D}}_3\boldsymbol{v}_1). \quad (29)$$

By comparing equations (28) and (29), we see that the order of operations is reversed. In equation (28), the partial derivatives terms are approximated by first interpolating and differencing, whereas in equation (29), the terms are first differenced and then interpolated. This particular discretization overcomes the issue that the interpolation and difference operators do not commute, which allows us to show that the scheme is energy conserving; see Appendix B. In equation (29) the off-diagonal terms are scaled by the Jacobian whereas the diagonal term is not. This scaling avoids requiring SBP interpolation operators that commute with the Jacobian to obtain an energy conservative discretization (O'Reilly and Petersson, 2020).

Discretization of boundary conditions

The traction-free boundary condition is weakly imposed by discretizing the penalty term in equation (15). In Appendix B, we show that the discretized penalty term can be absorbed into the $\mathcal{D}_k$ operators resulting in the modified operators $\tilde{\mathcal{D}}_k = \mathcal{D}_k - \mathcal{H}_{\mathbf{k}}^{-1}\mathcal{B}_k$. Therefore, to weakly impose the traction-free boundary condition, we set the penalty term to zero and replace $\mathcal{D}_k$ with $\tilde{\mathcal{D}}_k$ in the discretized momentum balance equations.

Application to irregular topography

The formulation in equations (11) and (12) is general in the sense that it can treat any type of curvilinear geometry that can be expressed by a continuously differentiable and nonsingular mapping. To apply the method to topography, we introduce the 1D mapping

$$x_1 = L_1 r^1, \quad x_2 = L_2 r^2, \quad x_3 = F(r^1, r^2, r^2). \quad (30)$$

The constants L_1 and L_2 define the length scales of the computational domain in the x_1 and x_2 directions, respectively. This 1D mapping significantly reduces the number of expensive mixed interpolation and differentiation operations to compute. In addition, we restrict attention to decomposable mapping functions F, such as

$$F(r^1, r^2, r^3) = f(r^1, r^2)g(r^3). \quad (31)$$

In equation (31), $0 \le g(r^3) \le 1$ is a monotonically increasing function that controls the distribution of grid points in the r^3 direction. The function $f(r^1, r^2)$ describes the shape of the free surface at the top side of the computational domain. All other sides of the computational domain are planar.

The mapping in equation (31) reduces the memory storage costs of the method while taking advantage of precomputation. In a general curvilinear formulation, the metric coefficients are usually stored as 3D arrays (unless they are repeatedly recomputed to save memory). In total, there are 10 such arrays (nine for the contravariant basis and one for the Jacobian determinant), and they all need to be evaluated at seven different grid positions (corresponding to the stress and velocity component positions). In contrast, the mapping in equations (31) allows us to precompute and store all of the metric coefficients as combinations of 1D and 2D arrays for all seven grid positions at a negligible cost.

By computing the covariant base vectors for the mapping in equations (30) and (31), we find

$$\mathbf{a}_1 = \begin{bmatrix} L_1 \\ 0 \\ g\frac{\partial f}{\partial r^1} \end{bmatrix}, \quad \mathbf{a}_2 = \begin{bmatrix} 0 \\ L_2 \\ g\frac{\partial f}{\partial r^2} \end{bmatrix}, \quad \mathbf{a}_3 = \begin{bmatrix} 0 \\ 0 \\ f\frac{dg}{dr^3} \end{bmatrix}.$$

The contravariant base vectors are

$$\mathbf{a}^1 = \begin{bmatrix} \frac{1}{L_1} \\ 0 \\ 0 \end{bmatrix}, \quad \mathbf{a}^2 = \begin{bmatrix} 0 \\ \frac{1}{L_2} \\ 0 \end{bmatrix}, \quad \mathbf{a}^3 = -\frac{1}{J} \begin{bmatrix} L_2 g \frac{\partial f}{\partial r^1} \\ L_1 g \frac{\partial f}{\partial r^2} \\ -L_1 L_2 \end{bmatrix}, \tag{32}$$

and the Jacobian determinant is

$$J = L_1 L_2 f \frac{dg}{dr^3}.$$

In the numerical scheme, we assume that the mapping function is only known at the corner points of each grid cell (see Fig. 1). Derivatives with respect to the mapping function are then approximated by appropriate combinations of SBP interpolation and differentiation operators.

NUMERICAL EXPERIMENTS

In this section, we conduct a series of numerical experiments to determine how to select the timestep, demonstrate the method's excellent stability properties, and determine the number of grid points per minimum wavelength required for resolving body and surface waves in topographic simulations. In all of the experiments, we advance in time using leap-frog timestepping.

Timestep selection

In an unbounded isotropic elastic medium, the fourth-order accuracy in space and second-order accuracy in time of the SGFD scheme satisfies the following Courant–Friedrichs–Lewy (CFL) condition (Graves, 1996)

$$\Delta t < \min \frac{\Delta x}{\sqrt{3} V_p (c_1 + c_2)} = C \min \frac{\Delta x}{V_p} \approx 0.495 \min \frac{\Delta x}{V_p}, \tag{33}$$

in which Δx is the uniform grid spacing (assumed to be the same in each grid direction), and $V_P = \sqrt{\lambda + 2\mu}/\sqrt{\rho}$ is the P-wave velocity. The condition in equation (33) applies for each grid point. Moreover, $c_1 = 9/8$ and $c_2 = 1/24$ are the coefficients of the FD stencil of the first derivative, and C is the CFL number.

Our model for bounding the maximum stable timestep of the curvilinear grid method depends on two different thresholds. The first threshold is an upper bound of the maximum stable timestep for grid directions or regions not experiencing a curvilinear grid transformation (e.g., the horizontal grid directions)

$$\Delta t < C_0 \min \frac{\Delta x}{V_p}, \tag{34}$$

in which $C_0 > 0$ is a constant to be determined. The second bound restricts the maximum stable timestep due to the curvilinear coordinate transformation in the vertical direction

$$\Delta t < C_1 \min \frac{h}{V_p \|\mathbf{a}^3\|_2}, \tag{35}$$

in which $h = 1/N$ is the grid spacing discretizing the unit interval, assuming $N + 1$ grid points. The norm $\|\mathbf{a}^3\|_2$ in equation (35) depends on the grid stretching, scaling effects, and the norm of the gradient of the topography function, f:

$$\|\mathbf{a}^3\|_2 = \frac{1}{|f g'|} \sqrt{1 + g \|\nabla f\|_2^2}, \quad \|\nabla f\|_2 = \sqrt{\left(\frac{\partial f}{\partial x_1}\right)^2 + \left(\frac{\partial f}{\partial x_2}\right)^2}. \tag{36}$$

When $\|\nabla f\|_2$ increases, Δt must decrease. Thus, large topographic gradients in f negatively impact the maximum stable timestep and may be poorly resolved on the grid. By combining the bounds in equations (34) and (35), we arrive at the following model for estimating the maximum stable timestep in our simulations

$$\Delta t < \min \left(C_0 \frac{\Delta x}{V_p}, C_1 \frac{h}{V_p \|\mathbf{a}^3\|_2} \right). \tag{37}$$

The constants C_0 and C_1 depend on the type of spatial discretization used (including the order of accuracy, use of SBP operators, and penalty terms). Furthermore, C_0 can only depend on the difference operators, whereas C_1 can depend on both difference and interpolation operators.

Because of the complexity of analytical derivation of C_0 and C_1 in equation (37), we bound the constants through numerical experiments from a set of simulations with randomly chosen topography profiles that range from small to large $\|\nabla f\|_2$. We generate a topography field that follows the von Karman spectral density function that takes the form

$$P_{vK}(k_x, k_y) = \frac{2^d \pi^{d/2} \epsilon^2 a_x a_y \gamma(\kappa + d/2)}{\gamma(|\kappa|)(1 + a_x^2 k_x^2 + a_y^2 k_y^2)^{\kappa + d/2}}, \tag{38}$$

in which d is the Euclidean dimension ($d = 2$ for a 2D field), γ is the gamma function, κ is the Hurst exponent ($\kappa = 0.8$), a_x and a_y are the correlation lengths in the x and y directions, and ϵ controls the magnitude of the fluctuations. We generate an isotropic topography field by letting $a_x = a_y = 2000$ m. The magnitude ϵ is irrelevant here because we normalize the generated topography field to make the elevation values fall between −1 and 1 m. The normalized model is then stretched vertically to generate topography fields with increasing maximum $\|\nabla f\|_2$. Our test models range from a flat topography (elevation = 0) to one with elevations ranging from −2560 to 2560 m. In each case, we search for the CFL number that lies on the boundary between a stable simulation and an unstable simulation. The stable simulations with the largest CFL number of the largest timestep are the ones that define the maximum stable timestep in each case. Figure 3 shows how the maximum stable timestep of each simulation depends on the ratio of the vertical deformation of the grid

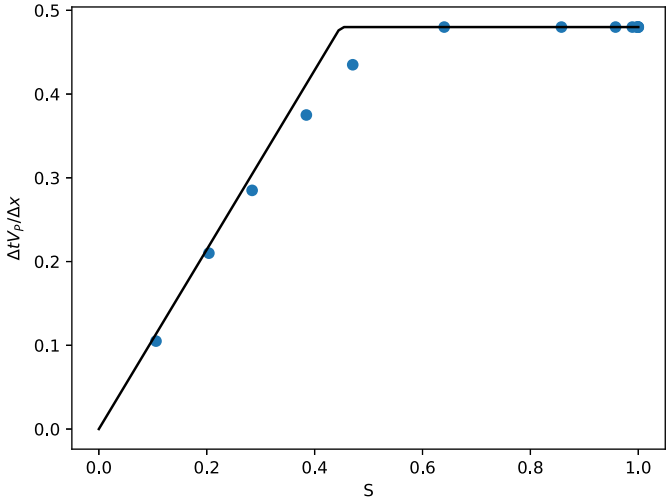

Figure 3. Normalized maximum stable timestep $\Delta t V_p/\Delta x$ as a function of $S = h/(\Delta x \|\mathbf{a}^3\|_2)$. Circles show the normalized maximum stable timestep obtained from simulations. Solid lines show the bound on the maximum stable timestep estimated by the equation. The color version of this figure is available only in the electronic edition.

spacing, due to topography, as a function of the uniform grid spacing,

$$S = \frac{h}{\Delta x \|\mathbf{a}^3\|_2}. \tag{39}$$

As S increases, the input grid geometry transitions from exhibiting large to small grid deformations. In the regime of large grid deformations (small S), the maximum stable timestep increases proportionally with S at a near-linear rate until it reaches a maximum, as predicted by equation (37). By applying a linear fit to the two simulation data points with the smallest S values, we find $C_1 \approx 1.07$. This constant is about a factor of 2 larger than the CFL number of the theoretical stability analysis in equation (33), which holds for a uniform grid in an unbounded domain. In the regime of small grid deformations, equation (34) bounds the maximum stable timestep with the CFL number $C_0 \approx 0.48$. This result is in good agreement with the theoretical CFL number $C \approx 0.50$ in equation (33). Therefore, we conclude that the design of the difference operators and the weakly imposed free surface boundary condition do not negatively impact the CFL number for uniform grid calculations in a significant way.

Energy conservation

We confirm that the numerical method is energy conservative by demonstrating that the energy rate over time fluctuates due to rounding errors only. The energy rate is numerically computed at each timestep by evaluating the sum of the kinetic and strain energy rates introduced in Appendix B. Because we discretize in time with leap-frog timestepping, these energy rates can be determined by knowing the numerical solution at the current $n+1$ and previous timestep n. In this case, the fully discrete approximation of the kinetic energy rate in equation (A13) is

$$\sum_i \boldsymbol{v}_i^T \boldsymbol{\rho}_i \mathbf{J}_i \mathbf{V}_i \frac{d\boldsymbol{v}i}{dt} \approx \dot{E}_k = \sum_i (\boldsymbol{v}_i^{n+1/2})^T \boldsymbol{\rho}_i \mathbf{V}_i \mathbf{J}_i \left(\frac{\boldsymbol{v}_i^{n+1/2} - \boldsymbol{v}_i^{n-1/2}}{\Delta t} \right).$$

Likewise, the fully discrete approximation of the strain energy rate in equation (B5) is

$$\sum_{i,j} \boldsymbol{\sigma}_{ij}^T \hat{\mathbf{J}}_{ij} \hat{\mathbf{V}}_{ij} \frac{d\epsilon_{ij}}{dt} \approx \dot{E}_s = \sum_{i,j} (\boldsymbol{\sigma}_{ij}^n)^T \hat{\mathbf{V}}_{ij} \hat{\mathbf{J}}_{ij} \left(\frac{\epsilon_{ij}^{n+1} - \epsilon_{ij}^n}{\Delta t} \right).$$

The energy rate is $\dot{E} = \dot{E}_k + \dot{E}_s$.

To test energy conservation of the numerical method, we generate a random media and topography using Gaussian white noise $Z \sim \mathcal{N}(0, \sigma)$ added to a homogeneous background model. The background model has density $\rho = 3.5$ g/cm^3, P wavespeed 6 km/s, and S wavespeed $V_S = 3.5$ km/s. We perturb the density by adding white noise with standard deviation $\sigma = 0.05\rho$. To guarantee that the stiffness tensor, defined in equation (A2), is positive definite everywhere, we add the same white noise realization with standard deviation $\sigma = 0.05 V_S$ to the wavespeeds. To generate the topography profile we generate white noise with standard deviation $\sigma = 100$.

The simulation is initialized by applying a moment tensor source in the center of the free surface (see the Double Couple at Depth section for details regarding the moment tensor source implementation). The only nonzero component of the moment tensor is m_{12}, and its rate is given by the step function

$$\dot{m}_{12} = \begin{cases} \dot{M}_0 & 0 < t \le t_0, \\ 0 & t > t_0. \end{cases} \tag{40}$$

In this experiment, the computational domain is 49.5 km × 49.5 km × 21.12 km excluding topography. We use $\dot{M}_0 = 10^{18}$ Nm/s, $t_0 = 2.5$ ms, grid spacing $h = 165$ m, and timestep $\Delta t = 2.5$ ms and advance in time until the final time of 2.5 s. Figure 4 shows that the energy rate at early times increases due to the constant-amplitude source in equation (40). Immediately after the time $t = 0.25$ s, the source vanishes and the energy rate abruptly approaches zero. At later times, the energy rate fluctuates around the mean $|\dot{\tilde{E}}|/|\dot{\tilde{E}}_k| \approx 3.5 \times 10^{-4}$ due to floating-point single-precision rounding errors.

Gaussian hill and canyon

We investigate the accuracy and stability of our numerical method using a Gaussian hill and canyon topography profile:

$$f(x_1, x_2) = L_3 + e^{-(x_1^2 + x_2^2)} - e^{-((x_1-10)^2 + (x_2-10)^2)} \text{km} \tag{41}$$

(see Fig. 5). For simplicity, we employ a linear grid stretching profile that extends to a depth of $L_3 = 21.12$ km. We focus on two experiments that share similar configurations but test different aspects of the method: (1) a double-couple source

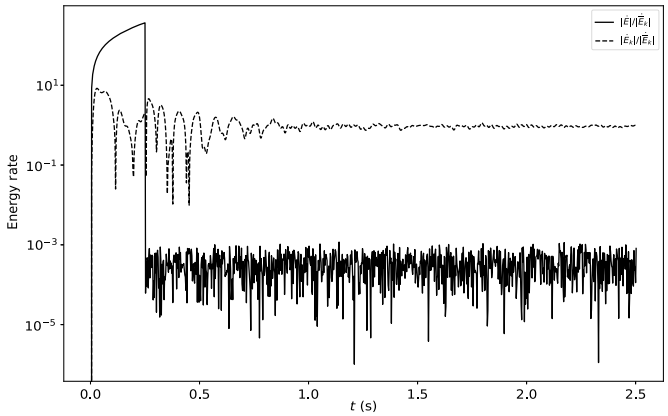

Figure 4. Test of energy conservation of the numerical scheme using randomly generated and uniformly distributed media parameters and topography elevation profile. Initially, the normalized energy rate increases due to the presence of a source term. After time $t = 0.25$ s, the source is no longer present, and the energy rate fluctuations are due to floating-point single-precision rounding errors.

buried below the Gaussian hill and (2) a point force applied on the summit of the Gaussian hill.

In each case, the source time function is the Ricker wavelet function

$$s(t) = (1 - 2\pi^2 f_p^2 (t - t_0)^2) e^{-\pi^2 f_p^2 (t-t_0)^2},$$

in which f_p is the peak frequency and t_0 is a time delay that prevents an abrupt onset. The source parameters and material properties used in both experiments are listed in Table 1.

To assess the accuracy, we define the minimum wavelength $\lambda_{\min} = V_S / f_{\max}$ using the shear-wave velocity V_S and maximum frequency $f_{\max}$ resolved on the grid. $f_{\max}$ is estimated using the frequency at which the Ricker wavelet reaches 5% of its peak amplitude in the frequency domain, $\approx 2.5 f_p$.

Double couple at depth. We use a double-couple source, buried 1 km below the summit of the Gaussian hill. In the Cartesian coordinate system, the source is located at the origin $\boldsymbol{x} = (0, 0, 0)s$. The double-couple source is zero for all moment tensor components m_{ij} except for component m_{12}. For this component, the moment rate is

$$\dot{m}_{12} = \dot{m}_0 s(t).$$

To handle the moment tensors in our implementation, we add the source term $-\dot{M}_{ij}$ to the right side of equation (14), in which

$$\dot{M}_{ij} = \frac{1}{J(r_s^1, r_s^2, r_s^3)} \dot{m}_{ij} \delta(r^1 - r_s^1) \delta(r^2 - r_s^2) \delta(r^3 - r_s^3). \quad (42)$$

In equation (42), $\mathbf{r}_s = (r_s^1, r_s^2, r_s^3)$ is the source location in parameter space.

This implementation requires finding the mapping of the physical coordinates to the parameter space coordinates. When the grid stretching function $g(r^3)$ is linear, the solution is trivial. Otherwise, one can apply Newton's method to solve for the parameter space coordinates. The Dirac delta function distribution applied in each direction is discretized to fourth-order accuracy by imposing moment conditions. If the source term is close to the boundary, the Dirac delta distributions must be discretized using the same quadrature rule as defined by the SBP operators. Otherwise, the source discretization is inaccurate.

The receivers are placed in a 5×5 grid at the free surface, which is centered around the summit of the Gaussian hill (see Fig. 5). In the horizontal plane, the receivers are 1 km apart in each direction.

Because the receiver locations do not coincide with the SG field locations, we interpolate the velocity field to each receiver location using cubic (fourth-order-accurate) Lagrange interpolation applied to the four nearest grid points for each field. The interpolation

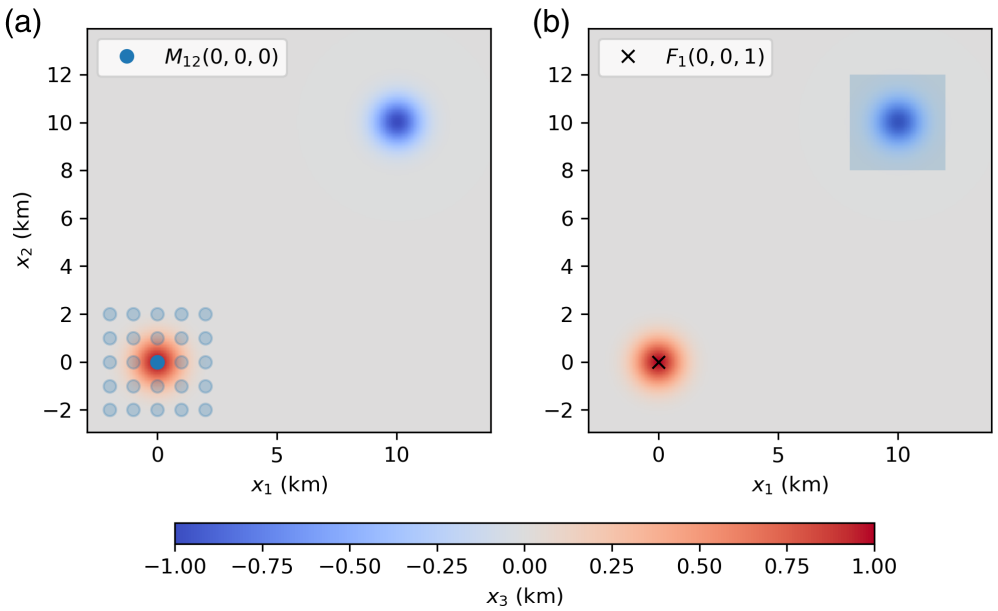

Figure 5. Map view of the Gaussian hill and canyon topography in Cartesian coordinates. (a) Location of (a) moment tensor source buried 1 km below the summit of the Gaussian hill and responses measured on a 5×5 grid (circles), and (b) point force applied on the summit of the Gaussian hill and computation of surface tractions covering the Gaussian canyon (shaded area). The color version of this figure is available only in the electronic edition.

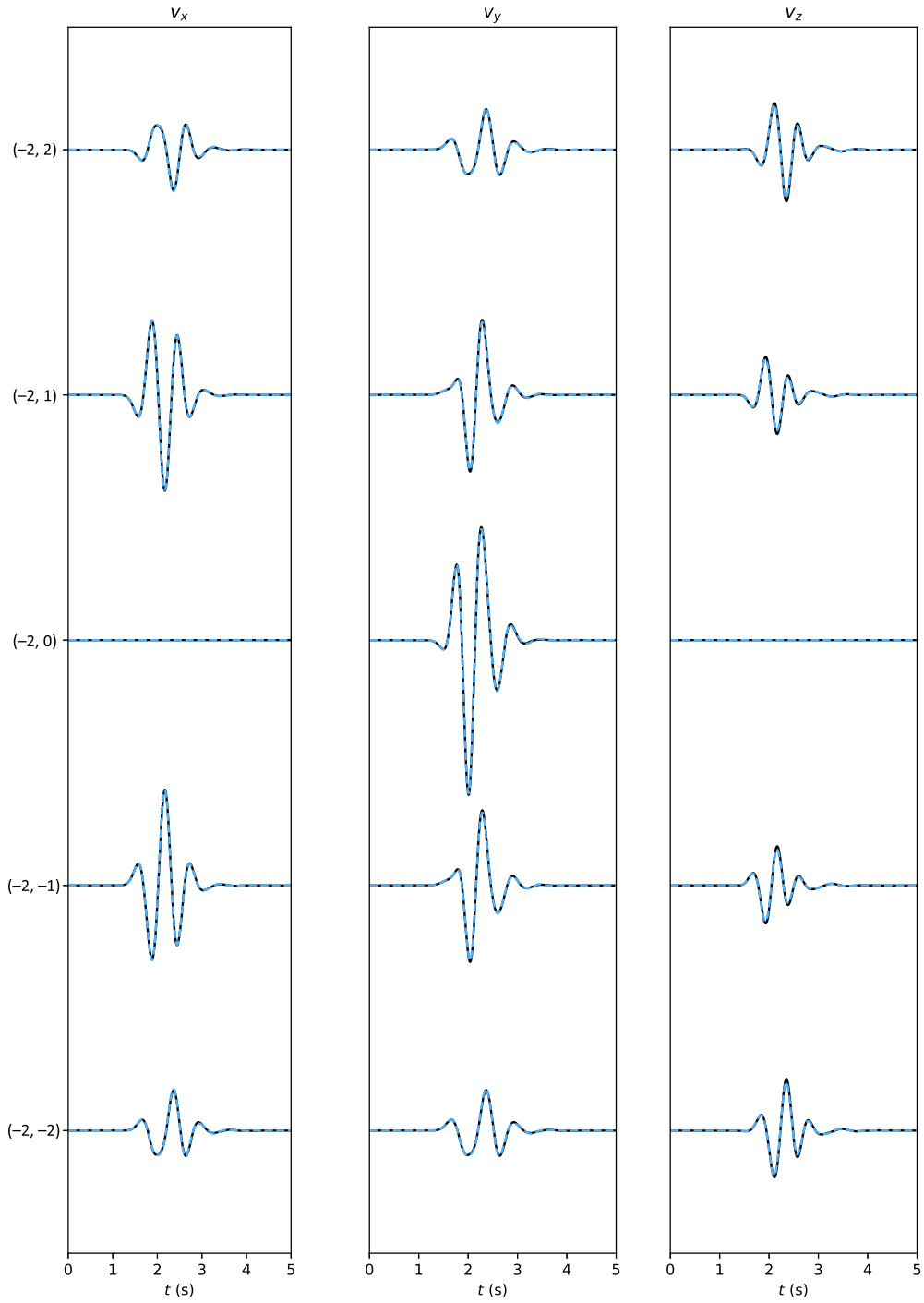

Figure 6. Comparisons of synthetic velocity waveforms computed using EDGE (solid traces) and the proposed curvilinear method (dashed traces) with six grid points per minimum *S* wavelength. The receivers are located along a line 2 km away from the Gaussian summit. The color version of this figure is available only in the electronic edition.

takes place in parameter space, not in physical space. Figure 6 shows good agreement between the numerical solution obtained by our code at $\lambda_{min}/h = 6$ and a DG solution EDGE (Breuer *et al.*, 2017). In this experiment, we used $h = 0.165$ km and timestep $\Delta t = 5$ ms.

Surface point force. Accurate simulation of surface waves is of great importance in many practical applications. To excite surface waves, we apply a point force on top of the Gaussian summit by introducing

$$\mathbf{F} = s(t)\mathbf{f}\delta(x_1)\delta(x_2),\ \mathbf{f} = \begin{bmatrix} f_1 \\ f_2 \\ f_3 \end{bmatrix}, \tag{43}$$

and impose the traction boundary condition $\mathbf{T} = \mathbf{F}(t)$ on the free surface. We discretize the boundary condition following the weak imposition of boundary conditions described in Appendix B. The Dirac distributions are again discretized by imposing moment conditions to achieve the fourth-order accuracy.

We set $f_1 = 10^{12}$ N and the other force components to zero. In addition, we set the grid spacing to $h = 0.1175$ km, corresponding to $\lambda_{min}/h = 8.5$ and $\lambda_{min,R}/h \approx 7.8$ when computing the minimum wavelength using the *S*-wave and Rayleigh wavespeed ($c_R \approx 3.21$ km/s), respectively. The timestep is the same as in the previous

TABLE 1
List of Source Parameters and Material Properties for the Gaussian Hill Problem

f_p (Hz)	t_0 (s)	$\dot{M}_0$ (N·m/s)	ρ (kg/m^3)	V_S (m/s)	V_P (m/s)
1.4	1.5	1018	2500	3500	6000

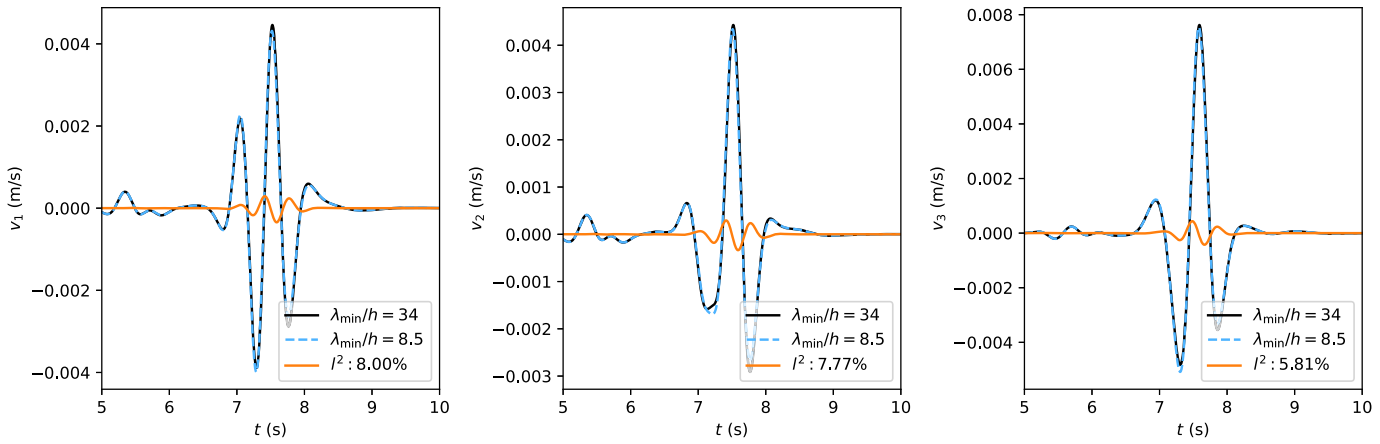

Figure 7. Particle velocity response measured at the bottom of the Gaussian canyon due to a point force applied on the summit of the Gaussian hill, computed using our numerical method at two different resolutions. The color version of this figure is available only in the electronic edition.

experiment, $\Delta t = 5$ ms. Figure 7 shows the particle velocity field at the bottom of the Gaussian canyon computed on a coarse grid and a fine grid with a factor of 4 grid refinement. The gain of less than 10% in the l^2 norm in time when compared against the fine-grid solution indicates that the coarse-grid results have already reached a relatively high accuracy in the presence of surface waves.

Increased accuracy in the modeling of surface waves by the curvilinear method may be obtained without a substantial increase in computational cost. The primary contribution to the error is most likely truncation errors present in the one-sided SBP FD stencils near the boundary. One way to reduce the boundary error is to introduce a nonuniform grid stretching function that clusters the grid points closer toward the boundary, but at the expense of decreasing the timestep. Another possibility is to raise the order of accuracy of the SBP operators to, for example, sixth- or eighth-order interior accuracy and third or fourth boundary accuracy.

Boundary error and convergence rates. Because the exact boundary conditions are known, the weak boundary conditions implemented in the numerical scheme provide an opportunity to estimate errors and convergence rates. To estimate the error on the boundary, we compare the traction-free boundary condition $\mathbf{T} = 0$ against the semidiscrete approximation of the traction vector. Because the scheme is convergent, the semidiscrete approximation of the traction vector must vanish with grid refinement. To approximate the traction vector at the position $(10 + \tilde{x}_1, 10 + \tilde{x}_2)$, we interpolate each component of the stress tensor to the fourth-order accuracy and evaluate the unit normal $\mathbf{n}$ with respect to the boundary. In the neighborhood of the Gaussian canyon, the Cartesian components of the normal are

$$n_1 = -2|n|^{-1}\tilde{x}_1 e^{-\tilde{x}_1^2-\tilde{x}_2^2}, n_2 = -2|n|^{-1}\tilde{x}_2 e^{-\tilde{x}_1^2-\tilde{x}_2^2}, \; n_3 = |n|^{-1},$$
$$|n| = \sqrt{4(\tilde{x}_1^2 + \tilde{x}_2^2)e^{-2\tilde{x}_1^2-2\tilde{x}_2^2} + 1}.$$

We quantify the error and convergence rate of the tractions in the L^2 norm using

$$e(t) = \sqrt{\frac{\sum_i \int_{\Omega_c} T_i T_i dS}{\sum_{i,j} \frac{1}{t_{end}} \int_{t=0}^{t_{end}} \int_{\Omega_c} \sigma_{ij}\sigma_{ij} dS dt}}. \quad (44)$$

By discretizing equation (44), we obtain an estimate of the L^2 error of the boundary traction as a function of time and normalized by stresses to obtain a dimensionless quantity. In the convergence study, the coarsest grid uses $\lambda_{min}/h = 8.5$ grid points per minimum S wavelength (or 7.8 grid points for Rayleigh waves), obtained with $h = 0.1175$ km and $\Delta t = 5$ ms. The subsequent grids use a factor of 2 grid refinement. The surface patch is $\Omega_c = [8, 12] \times [8, 12]$ km^2 and centered at the bottom of the Gaussian canyon. Figure 8 shows that the discrete approximation of equation (44) converges toward zero at a second-order convergence rate. We find that the error in the tractions is comparable to those estimated for the particle velocity fields shown in Figure 7. Hence, the error in tractions could potentially be used as an error control mechanism to identify which modes are adequately resolved in a simulation without requiring comparison against fine-grid or numerical solutions produced by other codes.

Reciprocity. We indirectly demonstrate the energy-conserving stability properties of our numerical scheme using a reciprocity test. Usually, one tests energy conservation of fully discrete approximation by confirming that, in the absence of sources and sinks, the discrete energy is positive for nonzero solutions and remains constant for long times. The reciprocity test does not require any energy computations, which

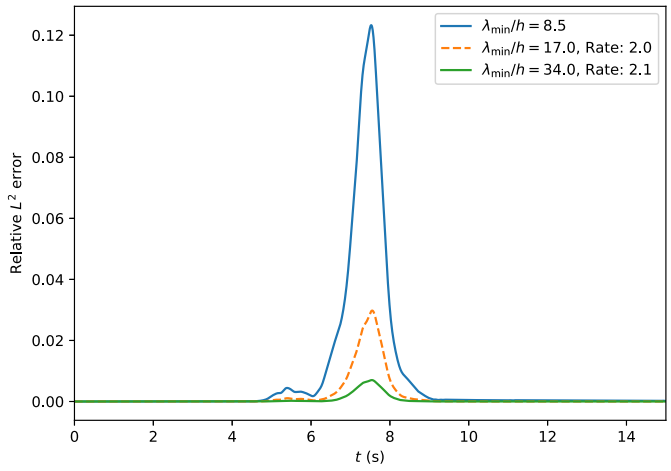

Figure 8. The L^2 norm of the discrete traction vector as a function of time measured over the patch Ω_c on the boundary, computed at three different grid resolutions. For a stable and weak imposition of the traction-free boundary condition, the discrete traction vector vanishes with grid refinement when $h \to 0$. The color version of this figure is available only in the electronic edition.

simplifies its implementation, but it needs to be carefully designed to be sensitive enough to detect potential instabilities.

Because the linear elastic wave equation is a self-adjoint linear operator, it follows that its Green's functions are symmetric in their arguments, that is, $G(x, y) = G(y, x)$. Because of the symmetry of the Green's function, it is possible to exchange source and receiver locations via a property known as *reciprocity*. Let $\mathbf{x}_s$ and $\mathbf{x}_r$ be source and receiver locations, respectively. Then, reciprocity implies that the response $v_k(\mathbf{x}_r, t)$ of a simulation with a moment tensor source M_{ij} can be reconstructed from a reciprocal simulation with a point force $F_k(\mathbf{x}_r, t)$ and measuring strains $\epsilon_{ij}^{(k)}(\mathbf{x}_s, t)$, using $v_k(\mathbf{x}_r, t) = \sum_{ij} \dot{M}_{ij} \epsilon_{ij}^{(k)}(\mathbf{x}_s, t)$. Because our method is energy conserving, the numerical Green's functions are also symmetric, and therefore reciprocity must hold in the discrete case, independent of accuracy. The implications of *accuracy-independent reciprocity* are that the reconstruction error $|v_k(\mathbf{x}_r, t) - \sum_{ij} \dot{M}_{ij} \epsilon_{ij}^{(k)}(\mathbf{x}_s, t)|$, when normalized, must be of the same order as floating-point rounding errors and must hold for any solution.

We demonstrate accuracy-independent reciprocity for a single component using the following model layout. For the forward simulation, a double couple $M_{12}(\mathbf{x}_s, t)$ is located at $\mathbf{x}_s = (10, 10, -1)$, and the response $v_1(\mathbf{x}_r, t)$ is recorded at $\mathbf{x}_r = (0, 0, 1)$. For the reciprocal simulation, the strains $\epsilon_{12}^{(1)}(\mathbf{x}_s, t) = \sigma_{12}^{(1)}(\mathbf{x}_s, t)/\mu$ are recorded for a point force $F_1(\mathbf{x}_r, t)$. Then, reciprocity implies that $v_1(\mathbf{x}_r, t) = \sigma_{12}^{(1)}(\mathbf{x}_s, t)/\mu$.

Because reciprocity must hold for any solution, we test using the same setup as before except that we increase the peak frequency f_p by an order of magnitude and use heterogeneous material properties. This increase causes severely under-resolved modes to be present in the numerical solutions. The heterogeneous material properties are defined by adding a linear perturbation of the form $(x + y + z)/h$ to each of the homogeneous density and wavespeed parameters. Despite having inaccurate numerical solutions, Figure 9 shows that the forward and reciprocal solutions only differ to single-precision rounding errors. Thus, this test demonstrates the strength of an energy-conserving method—stability of the numerical simulations is independent of the accuracy of the numerical solutions and is guaranteed (as long as the CFL condition is met) for any type of geometry. In numerical methods lacking proof of stability, instabilities often occur due to under-resolved modes that require artificial dissipation or filtering for suppression. The addition of artificial dissipation or filtering can stabilize the method, but may compromise accuracy.

Complex media and topography

The final verification test for our numerical method is a comparison with the solution by SPECFEM3D (Komatitsch and Vilotte, 1998; Komatitsch and Trump, 1999) for a highly

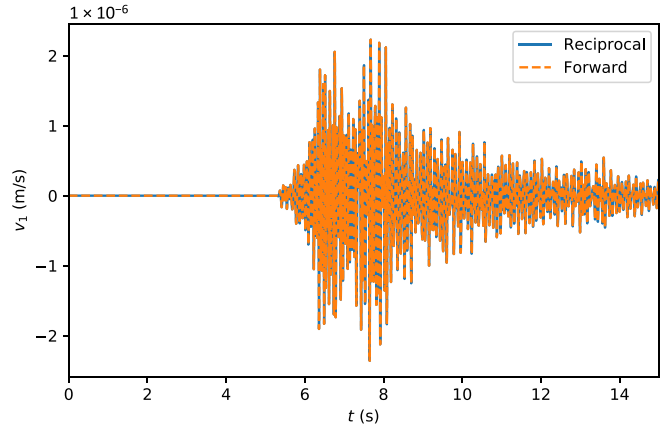

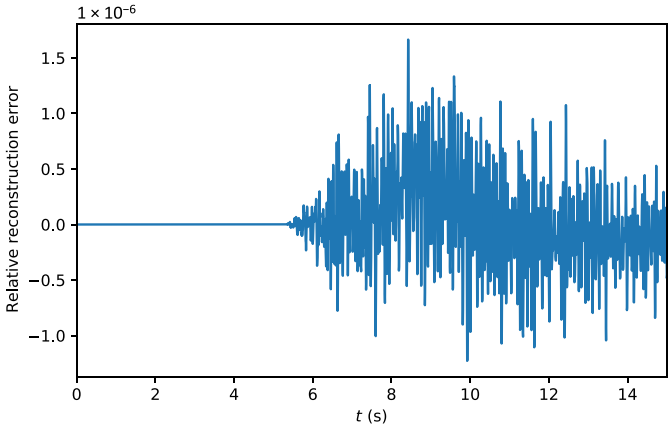

Figure 9. Reciprocity test using under-resolved numerical solutions computed in floating-point single precision. Because of having a provably stable method, the relative reconstruction error is exclusively determined by single-precision rounding error. The color version of this figure is available only in the electronic edition.

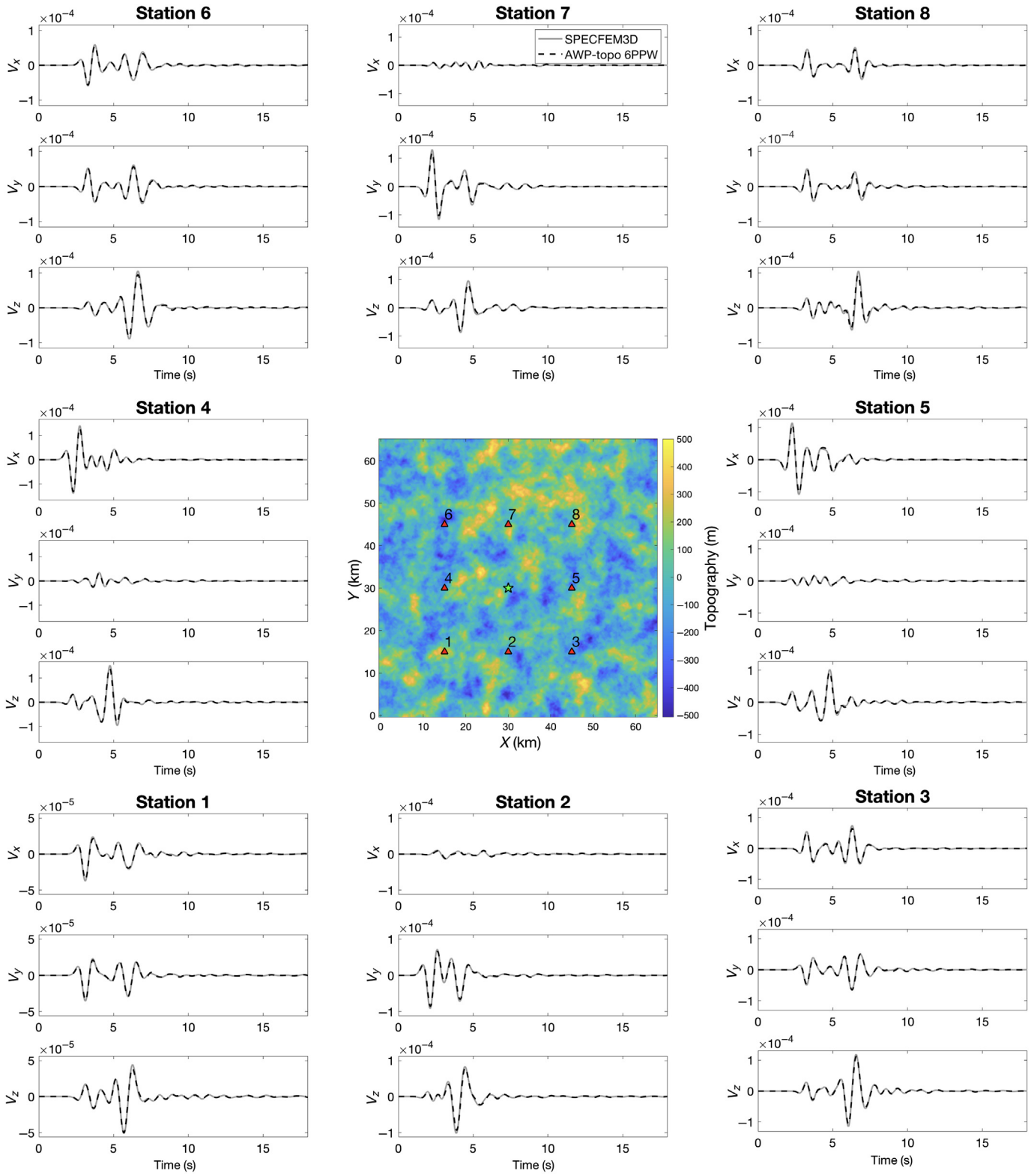

complex model with irregular topography. SPECFEM3D has been successfully applied to wave propagation simulations with complex surface topography directly incorporated into the spectral element mesh (Lee *et al.*, 2009). Here, we use a model of dimensions 65 km^3 with topography following a 2D isotropic von Karman power spectrum (equation 38) with a correlation length of 2 km (see Fig. 10, center). The topography

Figure 10. Comparisons of synthetic velocity waveforms computed using SPECFEM3D (solid traces) and the proposed curvilinear method (dashed traces) with six grid points per minimum *S* wavelength at receivers shown by the triangles on the map at the center. The shading of the map depicts the complex topography for the simulation; the star depicts the epicenter of the point source. The color version of this figure is available only in the electronic edition.

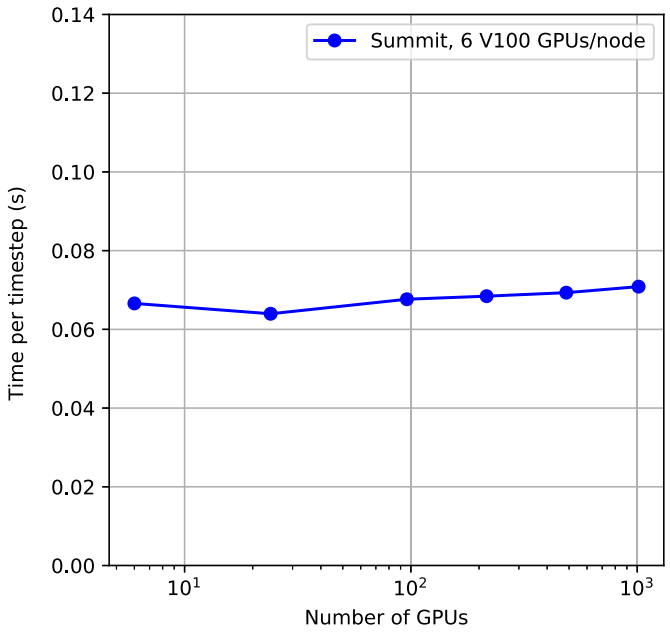

Figure 11. Weak scaling test of AWP conducted on Oak Ridge Leadership Computing Facility (OLCF) Summit. AWP achieves 94% weak scaling efficiency. The color version of this figure is available only in the electronic edition.

field is scaled to produce elevation values between −500 and 500 m. The topography is added on top of a heterogeneous medium, which is built by perturbing the top 9 km of a homogeneous background velocity structure ($V_P = 6000$ m/s, $V_S = 3464$ m/s, and $\rho = 2700$ kg/m^3) with a 3D von Karman noise field (10% standard deviation and correlation lengths of 1000 and 5000 m along vertical and horizontal directions, respectively). The mesh for the SPECFEM3D simulation is built with sufficiently high resolution to accurately describe the complex topographic interface and to ensure the convergence of the numerical solution. We use a constant intrinsic attenuation model for the test: $Q_P = Q_S = 50$. The simulation is initialized by a point source with an isotropic moment tensor ($m_{11} = m_{22} = m_{33} = 1.810^{15}$ N · m), located 1 km below the $z = 0$ level, near the center of the model. The source-time function is a Ricker wavelet with a maximum frequency of 2 Hz.

We compare the waveforms from the two solutions at receivers located 15–20 km from the source (see Fig. 10, center). To minimize location errors caused by the SG mesh, we discretize the source to fourth-order accuracy and interpolate the particle velocities at the receiver locations to fourth-order accuracy. The waveform comparisons show that the solution computed with our proposed method with a grid spacing of $\Delta x = 300$ m (six points per minimum S wavelength) is comparable to the reference solution at all receiver locations (Fig. 10). Additional tests with smaller grid spacings ensure the convergence of the numerical solution; thus the results indicate that our proposed curvilinear grid method provides sufficient accuracy in models with complex crustal structure as well as topography using at least six points per minimum S wavelength, at least for the propagation distances used here.

DISCUSSION AND CONCLUSIONS

We have implemented and verified support for complex topography in the high-order scalable AWP-ODC SGFD code using a curvilinear grid approach. AWP-ODC solves the 3D elastodynamic equations, including frequency-dependent anelasticity (Withers *et al.*, 2015) using memory variables. As opposed to many other proposed methods to incorporate topography into SGFD codes, our method is provably stable and therefore capable of handling any smooth topography without producing instability. In addition, the method requires relatively few points per minimum wavelength.

The Cartesian grid-based version of AWP-ODC has been extensively optimized and shows near-perfect scaling on thousands of GPUs (Cui *et al.*, 2013). Figure 11 shows a weak scaling test of curvilinear grid AWP with topography up to 1014 V100 GPUs on Oak Ridge Leadership Computing Facility Summit at 94% efficiency. This test uses a subdomain size of 300 × 1620 × 1280 grid points per node, or 150 × 540 × 1280 grid points per GPU. We selected this size by finding the maximum workload that fits onto a single GPU and varying the dimensions to find the configuration that yielded the best performance for a realistic application problem with 1280 grid points in the depth direction.

We have shown that our curvilinear approach to incorporate topography in high-order SGFD schemes does not negatively affect the maximum stable timestep on uniform grids. We constructed a simple model that bounds the maximum stable timestep depending on the magnitude of the contravariant basis in the vertical direction. This base vector depends on vertical grid cell stretching and spatial gradients in the topography profile. For sufficiently large spatial gradients, the maximum stable timestep has about a factor of 2 larger CFL number compared with the uniform grid case. This is because the terms in the scheme involving spatial gradients are discretized by combining interpolation and differentiation operators. The application of interpolation and differentiation in the same grid direction produces a wide and central collocated FD operator (O'Reilly and Petersson, 2020). Central collocated FD operators are less accurate than staggered operators, and they are prone to spurious oscillations due to inferior numerical dispersion properties. However, we have not encountered any spurious oscillations in our simulations with a broad range of realistic topographic variations. A possible future extension would involve replacing the collocated central stencils with compatible upwind stencils to suppress spurious oscillations while preserving discrete energy conservation in the numerical scheme (Mattsson and O'Reilly, 2018).

Nonlinear soil effects and fault-zone plasticity can strongly reduce ground-motion amplitudes for large earthquakes, even at longer periods, as demonstrated by Roten *et al.* (2014, 2016). Although the curvilinear grid AWP code does not currently include support for nonlinear rheology, such extension should be the focus of future work. Because evaluating the yield condition requires information on all components of the stress tensor, the staggering of the stress components complicates the implementation of plasticity even for planar surfaces (Roten *et al.*, 2016). Implementations of simple J2 plasticity (based on a von Mises or Drucker–Prager yield condition) will need to account for the stretching of the grid along the vertical axis during interpolation of stress tensor elements from adjacent grid locations. Future implementations of J2 plasticity in the curvilinear grid AWP code could be further developed into multisurface Iwan-type plasticity (Iwan, 1967), as has been done in the version of AWP with a horizontal free surface boundary condition (Roten *et al.*, 2018).

DATA AND RESOURCES

Plots and analysis in this article used the numeric computing environment MATLAB (www.mathworks.com, last accessed October 2020). SPECFEM3D was obtained from https://geodynamics.org/cig/software/specfem3d/#release (last accessed August 2021). EDGE was downloaded from https://github.com/3343/edge (last accessed August 2021). We provide example codes and summation-by-parts (SBP) operators in the repository available at github.com/ooreilly/sbp (last accessed August 2021).

DECLARATION OF COMPETING INTERESTS

The authors acknowledge there that are no conflicts of interest recorded.

ACKNOWLEDGMENTS

This research was supported by the Southern California Earthquake Center (SCEC; Contribution Number 11159). SCEC is funded by National Science Foundation (NSF) Cooperative Agreement EAR-1600087 and U.S. Geological Survey (USGS) Cooperative Agreement G17AC00047. Additional financial support was provided by the Pacific Gas and Electric Company. Computations in this project were performed on Summit, which is part of the Oak Ridge Leadership Facility at the Oak Ridge National Laboratory. The authors thank Guillaume Thomas-Collignon and Yifeng Cui for providing high-performance computing expertise.

REFERENCES

Aagaard, B. T., and R. W. Graves (2011). Testing long-period ground-motion simulations of scenario earthquakes using the M_w 7.2 El Mayor-Cucapah mainshock: Evaluation of finite-fault rupture characterization and 3D seismic velocity models, *Bull. Seismol. Soc. Am.* **101,** 895–907.

Almuhaidib, A. M., and M. N. Toksöz (2015). Finite difference elastic wave modeling with an irregular free surface using ADER scheme, *J. Geophys. Eng.* **12,** no. 3, 435–447.

Appelö, D., and T. Colonius (2009). A high-order super-grid-scale absorbing layer and its application to linear hyperbolic systems, *J. Comput. Phys.* **228,** no. 11, 4200–4217.

Arnold, D. N., F. Brezzi, B. Cockburn, and L. D. Marini (2002). Unified analysis of discontinuous Galerkin methods for elliptic problems, *SIAM J. Numer. Anal.* **39,** no. 5, 1749–1779.

Bayliss, A., K. E. Jordan, B. J. LeMesurier, and E. Turkel (1986). A fourth-order accurate finite-difference scheme for the computation of elastic waves, *Bull. Seismol. Soc. Am.* **76,** no. 4, 1115–1132.

Berenger, J.-P. (1994). A perfectly matched layer for the absorption of electromagnetic waves, *J. Comput. Phys.* **114,** no. 2, 185–200.

Breuer, A., A. Heinecke, and Y. Cui (2017). EDGE: Extreme scale fused seismic simulations with the discontinuous Galerkin method, *International Supercomputing Conf.*, Springer, 1–60.

Carpenter, M. H., D. Gottlieb, and S. Abarbanel (1994). Time-stable boundary conditions for finite-difference schemes solving hyperbolic systems: Methodology and application to high-order compact schemes, *J. Comput. Phys.* **111,** no. 2, 220–236.

Cerjan, C., D. Kosloff, R. Kosloff, and M. Reshef (1985). A nonreflecting boundary condition for discrete acoustic and elastic wave equations, *Geophysics* **50,** no. 4, 705–708.

Chung, E. T., C. Y. Lam, and J. Qian (2015). A staggered discontinuous Galerkin method for the simulation of seismic waves with surface topography, *Geophysics* **80,** no. 4, T119–T135.

Crouse, C. B., T. H. Jordan, K. R. Milner, C. A. Goulet, S. Callaghan, and R. W. Graves (2018). Site-specific MCER response spectra for Los Angeles region based on 3-D numerical simulations and NGA-West2 equations, *Proc. of the 11th National Conf. in Earthquake Engineering*, Earthquake Engineering Research Institute, Los Angeles, California.

Cui, Y., K. B. Olsen, T. H. Jordan, K. Lee, J. Zhou, P. Small, D. Roten, G. Ely, D. K. Panda, A. Choura-Sia, *et al.* (2010). Scalable earthquake simulation on petascale supercomputers, *Proc. Supercomputing Conf.*, New Orleans, Louisiana.

Cui, Y., E. Poyraz, K. B. Olsen, J. Zhou, K. Withers, S. Callaghan, J. Larkin, C. Guest, D. Choi, A. Chourasia, *et al.* (2013). Physics-based seismic hazard analysis on petascale heterogeneous supercomputers, *Proc. Supercomputing Conference*.

de la Puente, J., M. Ferrer, M. Hanzich, J. E. Castillo, and J. M. Cela (2014). Mimetic seismic wave modeling including topography on deformed staggered grids, *Geophysics* **79,** no. 3, 125–141.

Dovgilovich, L., and I. Sofronov (2015). High-accuracy finite-difference schemes for solving elastodynamic problems in curvilinear coordinates within multiblock approach, *Appl. Numer. Math.* **93,** 176–194.

Duru, K., and E. M. Dunham (2016). Dynamic earthquake rupture simulations on nonplanar faults embedded in 3D geometrically complex, heterogeneous elastic solids, *J. Comput. Phys.* **305,** 185–207.

Etienne, V., E. Chaljub, J. Virieux, and N. Glinsky (2010). An hp-adaptive discontinuous Galerkin finite-element method for 3-D elastic wave modelling, *Geophys. J. Int.* **183,** no. 2, 941–962.

Fernández, D. C. D. R., J. E. Hicken, and D. W. Zingg (2014). Review of summation-by-parts operators with simultaneous approximation terms for the numerical solution of partial differential equations, *Comput. Fluids* **95,** 171–196.

Gao, L., and D. Keyes (2019). Combining finite element and finite difference methods for isotropic elastic wave simulations in an energy-conserving manner, *J. Comput. Phys.* **378,** 665–685.

Gao, L., D. C. Del Rey Fernández, M. Carpenter, and D. Keyes (2019). SBP-SAT finite difference discretization of acoustic wave equations on staggered block-wise uniform grids, *J. Comput. Appl. Math.* **348,** 421–444.

Gassner, G. J. (2013). A skew-symmetric discontinuous Galerkin spectral element discretization and its relation to SBP-SAT finite difference methods, *SIAM J. Sci. Comput.* **35,** no. 3, A1233–A1253.

Givoli, D., T. Hagstrom, and I. Patlashenko (2006). Finite element formulation with high-order absorbing boundary conditions for time-dependent waves, *Comp. Methods Appl. Mech. Eng.* **195,** nos. 29/32, 3666–3690.

Gottschämmer, E., and K. B. Olsen (2001). Accuracy of the explicit planar free-surface boundary condition implemented in a fourth-order staggered-grid velocity-stress finite-difference scheme, *Bull. Seismol. Soc. Am.* **91,** no. B11309, 617–623.

Graves, R. W. (1996). Simulating seismic wave propagation in 3D elastic media using staggered grid finite differences, *Bull. Seismol. Soc. Am.* **86,** no. 4, 1091–1106.

Grinfeld, P. (2013). *Introduction to Tensor Analysis and the Calculus of Moving Surfaces*, Springer, New York, New York, 302 pp.

Hestholm, S. (2003). Elastic wave modeling with free surfaces: Stability of long simulations, *Geophysics* **68,** no. 1, 314–321.

Hestholm, S., and B. Ruud (1994). 2D finite-difference elastic wave modelling including surface topography, *Geophys. Prospect.* **42,** no. 5, 371–390.

Hestholm, S., and B. Ruud (1998). 3-D finite-difference elastic wave modeling including surface topography, *Geophysics* **63,** no. 2, 613–622.

Hestholm, S., and B. Ruud (2002). 3D free-boundary conditions for coordinate-transform finite-difference seismic modelling, *Geophys. Prospect.* **50,** no. 5, 463–474.

Hu, W. (2016). An improved immersed boundary finite-difference method for seismic wave propagation modeling with arbitrary surface topography, *Geophysics* **81,** no. 6, T311–T322.

Imperatori, W., and P. M. Mai (2015). The role of topography and lateral velocity heterogeneities on near source scattering and ground-motion variability, *Geophys. J. Int.* **202,** no. 3, 2163–2181.

Iwan, W. (1967). On a class of models for the yielding behavior of continuous and composite systems, *J. Appl. Mech.* **34,** no. 4, 612–617.

Janivita Joto Sudirham, J. J. S., J. J. Sudirham, J. J.W. van der Vegt, and R. M. J. van Damme (2003). *A study on discontinuous Galerkin finite element methods for elliptic problems*, *Mathematical Communications*, Imported from MEMORANDA.

Käser, M., and M. Dumbser (2008). A highly accurate discontinuous Galerkin method for complex interfaces between solids and moving fluids, *Geophysics* **73,** no. 3, T23–T35.

Komatitsch, D., and J. Trump (1999). Introduction to the spectral element method for three-dimensional seismic wave propagation, *Geophys. J. Int.* **139,** no. 3, 806–822.

Komatitsch, D., and J. P. Vilotte (1998). The spectral element method: An efficient tool to simulate the seismic response of 2D and 3D geological structures, *Bull. Seismol. Soc. Am.* **88,** no. 2, 368–392.

Kozdon, J. E., and L. C. Wilcox (2016). Stable coupling of nonconforming, high-order finite difference methods, *SIAM J. Sci. Comput.* **38,** no. 2, A923–A952.

Kozdon, J. E., E. M. Dunham, and J. Nordstrom (2013). Simulation of dynamic earthquake ruptures in complex geometries using high-order finite difference methods, *J. Sci. Comput.* **55,** no. 1, 92–124.

Kristek, J., P. Moczo, E. Chaljub, and M. Kristekova (2016). An orthorhombic representation of a heterogeneous medium for the finite-difference modelling of seismic wave propagation, *Geophys. J. Int.* **208,** no. 2, 1250–1264.

Lee, S.-J., D. Komatitsch, B.-S. Huang, and J. Tromp (2009). Effects of topography on seismic-wave propagation: An example from Northern Taiwan, *Bull. Seismol. Soc. Am.* **99,** no. 1, 314–325.

Levander, A. R. (1988). Fourth-order finite-difference *P-SV* seismograms, *Geophysics* **53,** no. 11, 1425–1436.

Lombard, B., J. Piraux, C. Gelis, and J. Virieux (2008). Free and smooth boundaries in 2-D finite-difference schemes for transient elastic waves, *Geophys. J. Int.* **172,** no. 1, 252–261.

Lundquist, T., A. Malan, and J. Nordström (2018). A hybrid framework for coupling arbitrary summation-by-parts schemes on general meshes, *J. Comput. Phys.* **362,** 49–68.

Mattsson, K., and M. H. Carpenter (2010). Stable and accurate interpolation operators for high-order multiblock finite difference methods, *SIAM J. Sci. Comput.* **32,** no. 4, 2298–2320.

Mattsson, K., and O. O'Reilly (2018). Compatible diagonal-norm staggered and upwind SBP operators, *J. Comput. Phys.* **352,** 52–75.

Mittet, R. (2002). Free-surface boundary conditions for elastic staggered-grid modeling schemes, *Geophys. J. Int.* **67,** no. 5, 1348–1672.

Nordström, J., K. Forsberg, C. Adamsson, and P. Eliasson (2003). Finite volume methods, unstructured meshes and strict stability for hyperbolic problems, *Appl. Numer. Math.* **45,** no. 4, 453–473.

Olsen, K. B., and C. Marcinkovich (2003). On the implementation of perfectly matched layers in a three-dimensional fourth-order velocity-stress finite difference scheme, *J. Geophys. Res.* **108,** no. B5, 2276, doi: 10.1029/2002JB002235.

Olsen, K. B., S. M. Day, and C. R. Bradley (2003). Estimation of Q for long-period (>2 s) waves in the Los Angeles Basin, *Bull. Seismol. Soc. Am.* **93,** 627–638.

Olsen, K. B., S. M. Day, L. Dalguer, J. Mayhew, Y. Cui, J. Zhu, V. M. Cruz-Atienza, D. Roten, P. Maechling, T.H. Jordan, *et al.* (2009). ShakeOut-D: Ground motion estimates using an ensemble of large earthquakes on the Southern San Andreas fault with spontaneous rupture propagation, *Geophys. Res. Lett.* **36,** L04303, doi: 10.1029/2008GL036832.

Olsen, K. B., S. M. Day, J. B. Minster, Y. Cui, A. Chourasia, M. Faerman, R. Moore, P. Maechling, and T. Jordan (2006). Strong shaking in Los Angeles expected from southern San Andreas earthquake, *Geophys. Res. Lett.* **33,** L07305, doi: 10.1029/2005GL025472.

Olsen, K. B., S. M. Day, J. B. Minster, Y. Cui, A. Chourasia, R. Moore, P. Maechling, and T. Jordan (2008). TeraShake2: Simulation of M_w 7.7 earthquakes on the southern San Andreas fault with spontaneous rupture description, *Bull. Seismol. Soc. Am.* **98,** 1162–1185.

O'Reilly, O., and N. A. Petersson (2020). Energy conservative SBP discretizations of the acoustic wave equation in covariant form on staggered curvilinear grids, *J. Comput. Phys.* **411,** 109386, doi: 10.1016/j.jcp.2020.109386.

O'Reilly, O., T. Lundquist, E. M. Dunham, and J. Nordstrom (2017). Energy stable and high-order-accurate finite difference methods on staggered grids, *J. Comput. Phys.* **346,** 572–589.

Peskin, C. S. (1972). Flow patterns around heart valves: A numerical method, *J. Comput. Phys.* **10,** no. 2, 252–271.

Prochnow, B., O. O'Reilly, E. M. Dunham, and N. A. Petersson (2017). Treatment of the polar coordinate singularity in axisymmetric wave propagation using high-order summation-by-parts operators on a staggered grid, *Comput. Fluids* **149,** 138–149.

Ranocha, H., J. Glaubitz, P. Offner, and T. Sonar (2018). Stability of artificial dissipation and modal filtering for flux reconstruction schemes using summation-by-parts operators, *Appl. Numer. Math.* **128,** 1–23.

Rodgers, A. J., N. A. Petersson, and B. Sjogreen (2010). Simulation of topographic effects on seismic waves from shallow explosions near the North Korean nuclear test site with emphasis on shear wave generation, *J. Geophys. Res.* **115,** no. B11309, doi: 10.1029/2010JB007707.

Roten, D., Y. Cui, K. B. Olsen, S. M. Day, K. Withers, W. H. Savran, P. Wang, and D. Mu (2016). High-frequency nonlinear earthquake simulations on petascale heterogeneous supercomputers, *Proc. Supercomputing Conf.*, Salt Lake City, Utah, 13–18 November.

Roten, D., K. B. Olsen, S. Day, and Y. Cui (2018). Implementation of Iwan-type plasticity model in AWP-ODC, *Poster Presentation at 2018 SCEC Annual Meeting*, Palm Springs, California, 8–12 September.

Roten, D., K. B. Olsen, S. M. Day, Y. Cui, and D. Fah (2014). Expected seismic shaking in Los Angeles reduced by San Andreas fault zone plasticity, *Geophys. Res. Lett.* **41,** 2769–2777.

Saenger, E. H., and T. H. Bohlen (2004). Finite-difference modeling of visco-elastic and anisotropic wave propagation using the rotated staggered grid, *Geophysics* **69,** no. 2, 583–591.

Sjögreen, B., and N. A. Petersson (2012). A fourth order accurate finite difference scheme for the elastic wave equation in second order formulation, *J. Sci. Comput.* **52,** no. 1, 17–48.

Spudich, P., M. Helweg, and W. H. K. Lee (1996). Directional topographic site response at Tarzana observed in aftershocks of the 1994 Northridge, California, earthquake: Implications for mainshock motions, *Bull. Seismol. Soc. Am.* **86,** no. 1B, S193–S208.

Sun, Y.-C., W. Zhang, and X. Chen (2018). 3D seismic wavefield modeling in generally anisotropic media with a topographic free surface by the curvilinear grid finite-difference method, *Bull. Seismol. Soc. Am.* **108,** no. 3A, 1287–1301.

Svärd, M., and J. Nordström (2014). Review of summation-by-parts schemes for initial-boundary-value problems, *J. Comput. Phys.* **268,** 17–38.

Takenaka, H., T. Nakamura, T. Okamoto, and Y. Kaneda (2009). A unified approach implementing land and ocean-bottom topographies in the staggered-grid finite-difference method for seismic wave modeling, *Proc. 9th SEGJ International Symposium*, October, 12–15.

Thompson, J. F., B. K. Soni, and N. P. Weatherill (1998). *Handbook of Grid Generation*, CRC press, Boca Raton, Florida, 1136 pp.

Tu, T., H. Yu, L. Ramirez-Guzman, J. Bielak, O. Ghattas, K.-L. Ma, and D. R. O'Halllaron (2006). From mesh generation to scientific visualization: An end-to-end approach to parallel supercomputing, *Proc. of the 2006 ACM/IEEE Int. Conf. for High Performance Computing, Networking, Storage and Analysis*, IEEE Computer Society, Tampa, Florida, 15 pp.

Withers, K., K. B. Olsen, and S. M. Day (2015). Memory efficient simulation of frequency dependent Q, *Bull. Seismol. Soc. Am.* **105,** 3129–3142.

Zeng, C., J. Miller, R. D. Xia, and G. P. Tsoflias (2012). An improved vacuum formulation for 2D finite-difference modeling of Rayleigh waves including surface topography and internal discontinuities, *Geophysics* **77,** no. 1, 1JF–Z19.

Zhang, W., Z. Zhang, and X. Chen (2012). Three-dimensional elastic wave numerical modelling in the presence of surface topography by a collocated-grid finite-difference method on curvilinear grids, *Geophys. J. Int.* **190,** no. 1, 358–378.

APPENDIX A
Energy balance

The elastic wave equation satisfies a mechanical energy balance that relates the total rate of energy change for an elastic medium to work done by external forces. If all of the boundaries are treated as traction-free surfaces, then the system's energy is conserved. When the boundary conditions are weakly imposed, the penalty parameter α in equation (16) can prevent the energy balance, unless appropriately chosen. We show here that $\alpha = 1$ conserves energy.

To define the mechanical energy of an isotropic elastic medium, it is convenient to first define the strain rate tensor,

$$\dot{\epsilon}_{ij} = \frac{1}{2}\sum_k \left(\frac{\partial v_i}{\partial r^k} a^{kj} + \frac{\partial v_j}{\partial r^k} a^{ki} \right). \tag{A1}$$

Stresses are related to strains and vice versa via Hooke's law and its inverse relationship,

$$\sigma_{ij} = \sum_{k,l} C_{ijkl}\epsilon_{kl}, \quad \epsilon_{ij} = \sum_{k,l} S_{ijkl}\sigma_{kl}, \tag{A2}$$

in which C_{ijkl} is the *stiffness tensor* and S_{ijkl} is the *compliance tensor*. For an isotropic elastic material, the time derivative of Hooke's law and its inverse relationship (without time derivative) are

$$\frac{\partial \sigma_{ij}}{\partial t} = \lambda \sum_{k,l} \frac{\partial v_k}{\partial r_l} a^{lk}\delta_{ij} + \mu \sum_l \left(\frac{\partial v_i}{\partial r^l} a^{lj} + \frac{\partial v_j}{\partial r^l} a^{li} \right), \tag{A3}$$

$$\epsilon_{ij} = \frac{\sigma_{ij}}{2\mu} - \frac{\lambda}{2\mu(3\lambda + 2\mu)} \sum_k \sigma_{kk}\delta_{ij}. \tag{A4}$$

The total mechanical energy for a linear elastic medium is the sum of its kinetic energy and strain (potential) energy

$$E = \frac{1}{2}\int \sum_i \rho_i v_i^2 + \sum_{i,j} \sigma_{ij}\epsilon_{ij} dV, \quad dV = J dr^1 dr^2 dr^3. \tag{A5}$$

Because $J > 0$, $\sigma_{ij}\epsilon_{ij} = \sum_{k,l} \sigma_{ij} S_{ijkl} \sigma_{kl}$, $E > 0$ for nonzero solutions implies that the compliance tensor is symmetric and positive definite.

We weakly impose the traction-free boundary condition on the entire boundary. By orthogonality (equation 6), the normal on the top boundary can also be expressed as

$$\mathbf{n} = \frac{J\mathbf{a}^3}{|\mathbf{a}_1 \times \mathbf{a}_2|}, \quad r^3 = 1. \tag{A6}$$

Using equation (A6), the traction vector is expressed in terms of the contravariant basis for a given side $r^k = 0, 1$ of the unit cube,

$$T_i^{(k)} = -\sum_j \sigma_{ij} \frac{Ja^{kj}}{A_k}, \quad r^k = 0, \tag{A7}$$

$$T_i^{(k)} = +\sum_j \sigma_{ij} \frac{Ja^{kj}}{A_k}, \quad r^k = 1. \tag{A8}$$

In equation (A8), $A_k = |\mathbf{a}_i \times \mathbf{a}_j|$, for $i \neq j \neq k$. The positive and negative signs in the traction vector come from the sign of the nonzero component of the outward unit normal with respect to each side $r^k = 0, 1$ of the unit cube. In the discrete case, we see that it is more convenient to work with a nonnormalized traction vector

$$\tilde{T}_i^{(k)} = A_k T_i^{(k)}. \tag{A9}$$

By expressing the lifting operator relation equation (17) in arithmetic form, we get

$$\int v_i \mathcal{L}(T_i) J dr^1 dr^2 dr^3 = \sum_k \int [v_i T_i A_k]_{r^k=0} + [v_i T_i A_k]_{r^k=1} dA_k, \tag{A10}$$

in which the $dA_k = \Pi_{l \neq k} dr^l$ is defined with respect to each side of the unit cube. The outward pointing unit normal changes sign depending on the side on which it acts. Thus,

$$\int v_i \mathcal{L}(T_i) J dr^1 dr^2 dr^3 = \sum_k \int [v_i \sigma_{ij} J a^{kj}]_{r^k=0}^{r^k=1} dA_k. \tag{A11}$$

We have the following result.

Lemma 1. If $\alpha = 1$, the elastodynamic equations (12) and (15), subject to the weak boundary condition in equation (16) conserve the energy in equation (A5) for all times $t \geq 0$.

Proof. Differentiating equation (A5) with respect to t leads to

$$\frac{dE}{dt} = \int \sum_i \rho v_i \frac{dv_i}{dt} J + \sum_{i,j} \sigma_{ij} \frac{d\epsilon_{ij}}{dt} J dr^1 dr^2 dr^3. \tag{A12}$$

By inserting equation (15) into equation (A12), the kinetic energy rate is

$$\int \sum_i \rho v_i \frac{dv_i}{dt} J dr^1 dr^2 dr^3 = \int \left(\sum_{i,k} v_i \frac{\partial}{\partial r^k} (J a^{kj} \sigma_{ij}) - \sum_i v_i \mathcal{L}(T_i) \right) J dr^1 dr^2 dr^3. \tag{A13}$$

By inserting equation (A1) into equation (A12), the strain energy rate is

$$\int \sum_{i,j,k} \sigma_{ij} \dot{\epsilon}_{ij} J dr^1 dr^2 dr^3 = \int \sum_{i,j,k} \sigma_{ij} \frac{\partial v_i}{\partial r^k} a^{kj} J dr^1 dr^2 dr^3. \tag{A14}$$

Combining equation (A13) and equation (A14) results in

$$\frac{dE}{dt} = \int \left(\sum_{i,j,k} \frac{\partial}{\partial r^k} (v_i \sigma_{ij} J a^{kj}) - \alpha \sum_i v_i \mathcal{L}(T_i) J \right) dr^1 dr^2 dr^3. \tag{A15}$$

In equation (A15), the first summand on the right side has been transformed using the product rule. By the fundamental theorem of calculus,

$$\int \sum_{i,j,k} \frac{\partial}{\partial r^k} (v_i \sigma_{ij} J a^{kj}) dV = \sum_{i,j,k} \int [v_i \sigma_{ij} J a^{kj}]_{r^k=0}^{r^k=1} dA_k, \tag{A16}$$

and the lifting operator equation (A11), the energy rate is solely determined by work done on the exterior boundaries

$$\begin{aligned} \frac{dE}{dt} &= (1-\alpha) \int \sum_{i,j,k} [v_i \sigma_{ij} J a^{kj}]_{r^k=0}^{r^k=1} dA_k \\ &= (1-\alpha) \sum_i \int_{\partial\Omega} v_i T_i dS. \end{aligned} \tag{A17}$$

Thus, the energy is conserved for $t \geq 0$ if $\alpha = 1$.

APPENDIX B
Energy balance of the semidiscrete problem

In this Appendix, we show that the traction-free boundary condition can be imposed by a simple modification of the summation-by-parts (SBP) operators in the momentum balance equation and that the numerical scheme satisfies an energy balance that mimics that of the continuous problem. A semidiscrete approximation of equation (11) is

$$\boldsymbol{\rho}_i \frac{d\mathbf{v}_i}{dt} = \mathbf{J}_i^{-1} \sum_{k,j} \boldsymbol{\mathcal{D}}_k \mathbf{G}_{ijk} \boldsymbol{\sigma}_{ij} - \mathbf{s}_i, \quad \mathbf{G}_{ijk} = \begin{cases} (\mathbf{J}\mathbf{a}^{ij})_{ij} & k = j \\ \boldsymbol{\mathcal{P}}_k (\mathbf{J}\mathbf{a}^{kj})_i \boldsymbol{\mathcal{P}}_i & k \neq j \end{cases}. \tag{B1}$$

This formulation splits the terms into two types: diagonal terms that can be discretized without any interpolation ($k = j$) and nondiagonal terms that must be interpolated ($k \neq j$).

Discretizing the lift operator definition (equation 17) and nonnormalized traction vector (equation A9) results in the following penalty term:

$$\mathbf{s}_i = \sum_k \mathbf{J}_i^{-1} \boldsymbol{\mathcal{H}}_{\mathbf{k}}^{-1} \tilde{\mathbf{T}}_i^{(k)}, \quad \tilde{\mathbf{T}}_i^{(k)} = \sum_j \boldsymbol{\mathcal{B}}_k \mathbf{G}_{ijk} \boldsymbol{\sigma}_{ij}. \tag{B2}$$

The boundary matrix $\boldsymbol{\mathcal{B}}_k$ takes the sign of the nonzero component of the outward pointing normal with respect to each side.

By inserting equation (B2) into equation (B1), the penalty term is absorbed into the difference operators

$$\rho_i \frac{d\boldsymbol{v}_i}{dt} = \mathbf{J}_i^{-1} \sum_{k,j} \underbrace{(\boldsymbol{\mathcal{D}}_k - \boldsymbol{\mathcal{H}}_{\mathbf{k}}^{-1}\boldsymbol{\mathcal{B}}_k)}_{\tilde{\boldsymbol{\mathcal{D}}}_k} \mathbf{G}_{ijk}\boldsymbol{\sigma}_{ij}. \tag{B3}$$

The SBP property (equation 24) can then be written as

$$\hat{\boldsymbol{\mathcal{H}}}_k \hat{\boldsymbol{\mathcal{D}}}_k = -(\boldsymbol{\mathcal{H}}_k \tilde{\boldsymbol{\mathcal{D}}}_k)^T. \tag{B4}$$

Following the same recipe, we can discretize the constitutive law (equation 12) (omitted for brevity). To derive the energy balance of the semidiscrete approximation, it is more straight-forward to work with the strain rate relationship (equation A1), which we discretize by

$$\frac{d\epsilon_{ij}}{dt} = \frac{1}{2}\sum_k (\mathbf{J})_{ij}^{-1} \hat{\mathbf{G}}_{ijk} \hat{\boldsymbol{\mathcal{D}}}_k \boldsymbol{v}_i + \frac{1}{2}\sum_k (\mathbf{J})_{ij}^{-1} \hat{\mathbf{G}}_{jik} \hat{\boldsymbol{\mathcal{D}}}_k \boldsymbol{v}_j,$$
$$\hat{\mathbf{G}}_{ijk} = \begin{cases} (\mathbf{J}\mathbf{a}^{ij})_{ij} & k = j \\ \hat{\boldsymbol{\mathcal{P}}}_j (\mathbf{J}\mathbf{a}^{kj})_i \hat{\boldsymbol{\mathcal{P}}}_k & k \neq j \end{cases}. \tag{B5}$$

We approximate the mechanical energy (equation A5) by

$$E_h = \frac{1}{2}\sum_i \boldsymbol{v}_i^T \mathbf{V}_i \mathbf{J}_i \boldsymbol{v}_i + \frac{1}{2}\sum_{i,j} \boldsymbol{\sigma}_{ij}^T \hat{\mathbf{V}}_{ij} \hat{\mathbf{J}}_{ij} \epsilon_{ij}. \tag{B6}$$

The diagonal matrices $\mathbf{V}_i$ and $\hat{\mathbf{V}}_{ij}$ are cubatures that contain the SBP quadrature weights at each grid location of the respective velocity and stress components

$$\mathbf{V}_1 = \mathbf{H}_1 \hat{\mathbf{H}}_2 \hat{\mathbf{H}}_3, \mathbf{V}_2 = \hat{\mathbf{H}}_1 \mathbf{H}_2 \hat{\mathbf{H}}_3, \mathbf{V}_3 = \hat{\mathbf{H}}_1 \hat{\mathbf{H}}_2 \mathbf{H}_3, \tag{B7}$$

$$\hat{\mathbf{V}}_{12} = \mathbf{H}_1 \mathbf{H}_2 \hat{\mathbf{H}}_3, \hat{\mathbf{V}}_{13} = \mathbf{H}_1 \hat{\mathbf{H}}_2 \mathbf{H}_3, \hat{\mathbf{V}}_{23} = \hat{\mathbf{H}}_1 \mathbf{H}_2 \mathbf{H}_3,$$
$$\hat{\mathbf{V}}_{11} = \hat{\mathbf{V}}_{22} = \hat{\mathbf{V}}_{33} = \hat{\mathbf{H}}_1 \hat{\mathbf{H}}_2 \hat{\mathbf{H}}_3. \tag{B8}$$

The energy E_h of the semidiscrete approximation satisfies the following result.

Lemma 2. The semidiscrete approximation in equations (B1) and (B5), with penalty term in equation (B2), conserves the energy (equation B6).

Proof. To simplify the analysis, we only consider the nondiagonal terms ($k \neq j$) in equations (B3) and (B5). Differentiating equation (A5) with respect to t and inserting equation (B1) into the result leads to kinetic energy rate

$$\sum_i \boldsymbol{v}_i^T \boldsymbol{\rho}_i \mathbf{J}_i \mathbf{V}_i \frac{d\mathrm{v}_i}{dt} = \sum_{i,j,k} \boldsymbol{v}_i^T \mathbf{V}_i \tilde{\boldsymbol{\mathcal{D}}}_k \boldsymbol{\mathcal{P}}_k (\mathbf{J}\mathbf{a}^{kj})_i \boldsymbol{\mathcal{P}}_j \boldsymbol{\sigma}_{ij}, \tag{B9}$$

and inserting equation (B5) into the result leads to the strain energy rate

$$\sum_{i,j} \boldsymbol{\sigma}_{ij}^T \hat{\mathbf{J}}_{ij} \hat{\mathbf{V}}_{ij} \frac{d\epsilon_{ij}}{dt} = \sum_{i,j,k} \boldsymbol{\sigma}_{ij}^T \hat{\mathbf{V}}_{ij} \hat{\boldsymbol{\mathcal{P}}}_j (\mathbf{J}\mathbf{a}^{kj})_i \hat{\boldsymbol{\mathcal{P}}}_k \hat{\boldsymbol{\mathcal{D}}}_k \boldsymbol{v}_i. \tag{B10}$$

By applying the SBP interpolation property (equation 25) twice, we can interchange the cubature and interpolation operators to obtain

$$\sum_{i,j} \boldsymbol{\sigma}_{ij}^T \hat{\mathbf{J}}_{ij} \hat{\mathbf{V}}_{ij} \frac{d\epsilon_{ij}}{dt} = \sum_{i,j,k} \boldsymbol{\sigma}_{ij}^T \boldsymbol{\mathcal{P}}_j^T (\mathbf{J}\mathbf{a}^{kj})_i \boldsymbol{\mathcal{P}}_k^T \hat{\mathbf{V}}_{ik} \hat{\boldsymbol{\mathcal{D}}}_k \boldsymbol{v}_i.$$

By taking the transpose, we find

$$\sum_{i,j} \boldsymbol{\sigma}_{ij}^T \hat{\mathbf{J}}_{ij} \hat{\mathbf{V}}_{ij} \frac{d\epsilon_{ij}}{dt} = \sum_{i,j,k} \boldsymbol{v}_i^T (\hat{\mathbf{V}}_{ik} \hat{\boldsymbol{\mathcal{D}}}_k)^T \boldsymbol{\mathcal{P}}_k (\mathbf{J}\mathbf{a}^{kj})_i \boldsymbol{\mathcal{P}}_j \boldsymbol{\sigma}_{ij}. \tag{B11}$$

We add the discrete kinetic and strain energy rates (equations B9 and B11) together to obtain the total mechanical energy in the system. Because of the SBP property in equation (B4), the discrete kinetic and strain energy rate balance each other

$$\frac{dE_h}{dt} = \sum_{i,j,k} \boldsymbol{v}_i^T (\mathbf{V}_i \tilde{\boldsymbol{\mathcal{D}}}_k + (\hat{\mathbf{V}}_{ik} \boldsymbol{\mathcal{D}}_k)^T) \boldsymbol{\mathcal{P}}_k (\mathbf{J}\mathbf{a}^{kj})_i \boldsymbol{\mathcal{P}}_j \boldsymbol{\sigma}_{ij} = 0. \tag{B12}$$

Manuscript received 30 March 2021
Published online 7 September 2021